Experimental and numerical study of nanosecond pulsed water-containing discharges

A DISSERTATION

SUBMITTED TO THE FACULTY OF THE GRADUATE SCHOOL

OF THE UNIVERSITY OF MINNESOTA

BY

Yuchen Luo

IN PARTIAL FULFILLMENT OF THE REQUIREMENTS

FOR THE DEGREE OF

DOCTOR OF PHILOSOPHY

Advisor: Peter J. Bruggeman

July 2019

© Yuchen Luo 2019

ALL RIGHTS RESERVED

Acknowledgements

It has been six years since I first set my feet in the beautiful University of Minnesota campus. Till today I can still remember the mixed feeling of exciting and nervous. It was not easy for me to choose a supervisor to work with at the beginning of my PhD study. I was not sure about what my interest was and what field I would like to work in for the next five to six years. After I talked to many professors from different departments and rotated in several different labs for one and half years, I finally joined Professor Bruggeman's group.

Professor Bruggeman is a very considerate person and supervisor. He cares about his student not only in terms of research progress, but also in the personal wellbeing and development. He encourages me to pursue my true interest and always opens his door for me to have a drop-by discussion. In his group, I worked towards my goal as a professional researcher and learned to think critically and systematically when facing a research problem. Without his help, I cannot finish my PhD study.

I learned a lot from the interaction with other researchers in the field as well. Dr. Shurik Yatom provided his TaLIF measurement of atomic H in the plasma jet to me and guided me into the experimental physics filed. Shurik was patient with me when I had very little experience in doing experiment and messed up with his setups. I am really grateful to have him in the lab to teach me experiment basics. With the discussion with Mr. Gaku Oinuma, a visiting scholar in our group, I learned how to control the generation of helium bubbles in the water. Gaku is a very knowledgeable plasma physicist and very professional researcher. It was very delightful to work with him in a project and learn from him. After a short visit to Professor Mark J. Kushner's group, I learned how to use Globalkin and installed it in our university's MSI system. Professor

Mark J. Kushner and Dr. Amanda M. Lietz gave me tremendous help during my visit and replied my emails with very detailed explanation. I would like to especially thank Professor Mark J. Kushner and Dr. Amanda M. Lietz for being such a great help to teach me use Globalkin. Mr. Vighneswara Siva Santosh Kumar Kondeti in our group offered me great help in setting up the LIF laser system and shared his data processing program with me. Santosh was a great help to me and I really appreciate that. Dr. Marien Junior Simeni Simeni in our group provided his experimental image of a corona discharge in water for me to use and always held meaningful and interesting discussion with me about the topic of plasma in liquid. I enjoyed the conversation with him very much. Dr. Florent P. Sainct generously provided his pure water vapor experimental data for me to use as a validation for my pure water vapor model which saves me lots of time of reading data from the published papers. The other former and current group members Mr. Sampson Moore, Mr. Gaurav Nayak, Mr. Jingkai Jiang and Mr. Chuanjie Chen helped me in the lab and gave me very helpful suggestions in my research. I would like to thank them as well. Mr. Mike Jensen and Mr. Ron Bystrom in the CSE machine shop provided lots of insightful suggestions to improve my experimental setup design and manufactured them in high quality. With their help, the experiment went well.

Last but not least, I would like to thank my parents. They are always there for me. They are happy for my success and encourage me when I fail. We went through all the ups and downs for all these years and they are always supportive and let me to pursue my dreams. Mom and Dad, I love you.

Dedication

To my family

Abstract

Water-containing discharges have been extensively studied for their potential in environmental remediation and biomedical applications. Highly reactive OH radicals are abundantly produced in the presence of water discharges enabling the oxidation and dissociation of harmful compounds and pollutants or the deactivation of bacteria and viruses. Although water-containing discharges can be highly effective for these applications, the energy efficiency is often a bottleneck, particularly for direct liquid discharges, for the wide industry-level applications of the water-containing discharges for environmental remediation. The goal of this study is to understand the OH production and destruction mechanism in the water-containing discharges within the framework of improving the energy efficiency of the water-containing discharges, especially for discharges directed generated in the liquid water.

The OH production and destruction mechanism in the low electron density (n_e ~ 10^{18} m^{-3}) gas phase discharges have been extensively studied. The electron-induced water dissociation is responsible for OH production and three-body recombination of OH with OH and H are the major loss mechanisms. However, the OH production and destruction mechanisms in the high electron density (> 10^{22} m^{-3}) gas phase discharges is not well understood, let alone the OH production and destruction mechanisms in liquid water in which electron density up to 10^{25} m^{-3} has been observed. These higher electron density discharges are important for many applications as most applications involve filamentary discharges with often high specific energies and electron densities. A plasma jet with gas shielding has been implemented to achieve a stable plasma filament with a high electron density in argon with added water vapor. For this study, the water concentration was kept within 1%. The discharge was

stabilized in time and space using a pin-to-plate geometry. The time resolved OH density was measured using laser induced fluorescence (LIF). The measured OH radical densities together with previously measured H densities by two-photon laser induced fluorescence (TaLIF) were used to validate a reaction set with a global 0-D plasma kinetics model. The model indicates that at high energy density the increase of atomic H and O densities lead to rapid radical recombination mainly producing H_2, O_2 and H_2O. A higher selectivity and energy efficiency for H_2O_2 production occurs at lower discharge energies for concentrations of water ranging from 0.1% t0 100%. Total H and O radical production increase with increasing power (or energy) deposition regardless of conditions until H_2O is depleted, nonetheless for OH radical there is a transition point observed at higher power densities. When the power density exceeds the corresponding power at the transition point, the H and O radical can be significantly larger than the OH density. This is due to the large electron density leading to electron-induced dissociation of OH during the voltage pulse.

The radial distribution of the OH fluorescence intensity in and near the plasma filament was also obtained by LIF measurement. A local minimum of OH fluorescence intensity at the position of the plasma filament was observed. This is ascribed to high O and H density leading to a much shorter lifetime of the OH radical in the filament compared to the surrounding of the filament. The H and O, present at significantly higher densities than the OH densities, diffuse out from the discharge core during the afterglow and produce OH in the immediate surrounding of the discharge filament.

The reaction set was further extended to enable its use for nanosecond pulsed discharges in pure water vapor by adapting reaction rates for high temperature and including thermal dissociation reactions. Fast gas heating leads to

significant pressure build up within tens of nanosecond and a two-stage simulation was used to calculate the kinetics during pressure build up and the kinetics after pressure relaxation due to shock wave relaxation. The pure water vapor discharges kinetics was compared with previously reported measured electron density, gas temperatures and H_2 production. In the case of high electron density pure water vapor kinetics, the H and O density even exceed the electron density during the discharge. As a result, OH radical is produced during the discharge by H and O reaction in good approximation balancing the electron-induced dissociation of the OH radicals leading to similar densities of H, O and OH. The OH density is not so significantly consumed during the high electron density pure water vapor discharges as in the high electron density Ar discharges with small water vapor concentrations.

Although a key interest is understanding the kinetics of direct liquid phase discharges, the small length scales, often random and irreproducible formation of discharge filaments and changes in refractive index make laser diagnostics extremely challenging. To enable future advanced optical diagnostics for discharge in bubbles and direct liquid phase discharges in water we developed two experimental setups. We developed a bubble generation system synchronized with multi-pulse discharge capabilities and performed imaging and electrical measurements. Surprisingly, due to the surface discharge accumulation at the quartz tube wall a memory effect is observed which leads to a reduction of the discharge intensity with increasing discharge repetition rate. We have also developed a reactor enabling the formation of controlled nanosecond pulse discharge in liquid water. A major challenge for this setup is to measure the power deposition accurately since an accurate power waveform is a crucial input parameter to plasma kinetics models. We developed and manufactured an embedded power

measurement system, including a voltage and current sensor. The home-made sensors can achieve a nanosecond resolution measurement and provide a clear waveform till tens of microsecond. Even the nanosecond voltage is usually applied in the generation of the liquid water discharge, the oscillation and reflection can last for several microsecond which produces re-ignitions of the plasma. The developed bubble and direct liquid water discharge reactor with preliminary characterization will allow for the development of more accurate and detailed measurements in the future which will without doubt enhance further our understanding of these discharges.

Table of Content

List of Tables

List of Figures

1 Introduction

1.1 Introduction to plasmas

Plasma is an ionized gas (or liquid) consisting of charged particles (electron and ions), photons and neutral atoms and molecules, including excited species, radicals and ground state atoms and molecules. Despite the possible large concentrations of charged species, the bulk of the plasma remains charge neutral. Laboratory plasmas are typically driven by electrical energy transfer from an electric field to the electrons and ions in the sheath. The free electrons in the plasma have orders of magnitude smaller mass compared with other heavy particles and can respond almost instantaneously to the external applied electrical field, gaining most of the electrical energy in the bulk of the plasma. The energy loss by the electrons is through collisions with heavy particles. Elastic collisions lead to inefficient momentum transfer to neutral and inelastic collisions can lead to excitation, ionization and dissociation of molecules. Radicals, highly reactive species that enable many plasma processes, are produced through electron-induced dissociation of molecules.

In the case of low-pressure plasmas (mTorr – Torr range) the collision frequency is low and energy transfer from electrons to neutrals is much slower than the energy transfer from the electric field to the electrons. In this case it is relatively easy to generate plasmas with near room temperature gas temperatures and electron energies of several eV. However, for atmospheric pressure plasmas, the collision frequency is orders of magnitudes higher and the energy transfer from the electrons to the neutral heavy particles occurs on timescales of the order of hundreds of nanoseconds. [1] If the amount of energy added is on a nanosecond time scale, energy is only transferred to the

electrons and collision energy transfer from electrons to neutrals is mainly through inelastic collisions leading to highly non-equilibrium plasmas ($T_e >> T_g$). In this case, the mean energy of the electrons is much higher than the mean energy of the background gas molecules, which can remain close to room temperature. When the plasma excitation process is extended to larger time scale, gas heating is typically not negligible, and the gas temperature will increase ultimately leading to a thermal equilibrium. In this thesis, nanosecond non-equilibrium atmospheric pressure discharges are studied enabling the production of highly non-equilibrium plasmas in atmospheric pressure plasmas in the gas phase and even in liquids.

1.2 Background

Pollution is a major challenge for our society and will increasingly be so if no action is taken. Plasma is a technology with huge potential to remediate pollution related issues at the source. While many examples exist of plasmas being used for air treatment applications [2, 3], plasma treatments of water except for ozone treatment, have not been implemented on a large scale nonetheless many promising laboratory studies are reported [4, 5]. Electrical discharge plasma in or in contact with liquid water can be used to deal with a wide range of chemical compounds and pollutants including complex organic dyes, phenols, chlorinated compounds, and pharmaceuticals [4, 6]. From the current knowledge and research, destruction of chemical compounds and inactivation of bacteria are the two important applications of plasma in and contact with liquid water. Plasmas in contact with water usually refer to plasma generated in the gas phase with liquid water used as one of the electrodes. Plasmas can also be generated directly in liquid water [7, 8].

The energy efficiency of high electron density water-containing discharges is

currently low, especially for discharges generated in pure water. As shown in [9], for dye treatment, the most energy efficient plasma processing method is pulsed corona discharge in the gas phase. The energy efficiency of dye destruction by direct discharges in water is quite low. Phenol, chloro- and nitro-phenols, atrazine and TNT can also be processed using direct plasma discharges generated in water but with a very low energy efficiency compared to decoloration of dyes [9].

In general, sustaining discharges in the gas phase requires less energy compared to discharges produced directly in liquid phase. This is typically ascribed to the higher breakdown voltage in liquids, and specifically for water to the large thermal heat capacity and latent heat involved in the evaporation of the water in and near the plasma filament [10]. While gas phase plasma can be generated with much less energy, the reactive species generated in the gas phase need to be transported to the liquid water and as short-lived radicals are often the key species enabling the treatment of chemical compounds, the process is highly transport limited. If the reactive species can be produced in the water with better energy efficiency, an improved transportation of radicals to the targeted position compared to gas phase plasmas is to be expected.

In order to make plasma processing technology for water treatment a sustainable solution to remediate environmental pollution, its energy efficiency should be comparable to the competitive advanced oxidation technologies (AoTs) including direct ozone treatment, Fenton's method, direct UV and various other combinations of ozone, H_2O_2, UV and catalysts. Plasma produces ozone, UV, OH radicals, H_2O_2 and even shock waves. The comparison of plasma with other AOTs for special applications allows us to assess the usefulness for specific environmental remediation processes. In

general, for high concentrations and highly toxic pollutants, thermal plasma is a better choice, as it provides a full conversion of the pollutant at high energy cost. For low concentration of pollutants, non-thermal plasma is used, which provides a significant reduction but incomplete conversion of the pollutant at low energy cost.

Apart from water treatment, plasma is also actively studied for bacterial disinfection. There are several factors influencing the efficiency of plasma bacterial disinfection, including plasma characteristics, bacterial type, and the transport of reactive species to and within the water sample.

The process of plasma-water interaction is reviewed in a more fundamental way in [11]. Lots of groups have published papers to show their research on plasma when interacting with water by studying the electron densities and gas temperatures. The results may strongly vary for different operating conditions and the configuration of plasma reactors. Different plasma-liquid interaction approaches are estimated by energy efficiency and effective action in [9] in order to give the community a way to focus on the most promising plasma to be used in the industry and be commercialized. At least one order of magnitude of increase in energy efficiency of plasma interacting with water is still required to make it a commercial large-scale viable process for water treatment [9].

1.3 Motivation and objective

To understand the reason for low energy efficiencies of direct water discharges, more sophisticated diagnostic methods for reactive species and more accurate plasma properties measurements become very important and with urgent need. The research towards obtaining accurate plasma properties has not been very well developed for plasma produced in liquids. This is due to the

complexity of the plasma interaction with liquid water. The diagnostic techniques for plasma in the water need high temporal and spatial resolution due to the fast ionization process and small dimensions of plasma filaments (~ 10 μm). The plasma, while initially can be produced in the liquid phase is in many cases in a gas or vapor phase while the surroundings are liquid phase, hence there will be large temperature and density gradients. The plasma can reach gas temperatures of thousands of Kelvin while the bulk water remains at room temperature.

In addition, large amount of reactive and excited species are the products during plasma-water interaction, with lifetime ranging from picosecond, such as electrons (electrons are solvated in water on picosecond time scales), to hours, such as H_2O_2, and with characteristic diffusion length scale ranging from nm to cm. These wide ranges of temporal and spatial resolution bring challenges to both diagnostics and modelling to understand the plasma directly generated in water. How to avoid the challenging multiphase plasma water interaction problem while still be able to obtain properties of the water-containing discharges becomes an important scientific question to answer. Currently almost all the studies of discharges in the water are using microsecond pulsed voltage generators. Only very limited number of experiments are employing nanosecond pulsed voltage generator in plasma in water experiment [12]. Nanosecond pulsed voltage generators have advantages to generate plasma in the water compared with microsecond pulsed voltage generator. The potential merits of nanosecond pulse generator can be summarized as: lower heating effect, higher electric field in the plasma and more efficient radical species produced by plasma-induced chemistry. It provides also a better temporal control of the discharge generation for diagnostics

More fundamental studies are needed to focus on nanosecond discharges in the water. Some research has been done to study the plasma characteristics, such as electron densities, gas temperatures and radical formation mechanisms in the past decade. Direct plasma discharges in liquid water can have an electron density 10^{24} ~ 10^{25} m^{-3}. The dissociation rate of the liquid water in the plasma region can be very high and in the plasma region all species are in the gas phase. Laser diagnostics to probe radical generation in liquid phase discharges are extremely challenging and to this end it is valuable to study similar plasmas in the gas phase that enable accurate radical species density measurements. An approach is to dilute the water concentration with an inert gas such as Ar to enable the study of water vapor kinetics at moderate gas temperatures while having a large electron density and dissociation degree ~100%. This leads to similar chemical reaction kinetics between this condition and pure water liquid discharges and enables us to perform a reaction set validation. A first step towards the overall goal to understand the plasma kinetics in the pure water plasma is to develop and validate predictive modeling capabilities in the low water concentration gas phase discharge and then extrapolate the model and understanding to the pure water kinetics.

Since atmospheric nonequilibrium high electron density water-containing discharges are usually filamentary and transient in nature, the discharges need to be stabilized first before any temporal and spatially resolved diagnostics can be performed. For the water-containing gas phase discharge with inert gases as the carrier gas, we generated the plasma between a pin and plate electrode with a gas flow to spatially stabilize the filament. The discharge was sustained by nanosecond pulsed voltage sources providing temporal control of the discharge generation.

While for gas phase discharges, voltages up to 10 kV can generate discharges in mm gaps, the large dielectric constant and 3 orders of magnitude higher density of liquid water requires voltage pulses with a magnitude as high as 50 kV and rise-times as short as 3 ns or even ps in the generation of discharge. Once the discharge is stabilized, the next challenge is to measure important plasma properties, such as the power density, the electron density, the electron temperature and the gas temperature. All these properties determine the plasma kinetics of the discharge. In addition to enable us to gain understanding of the plasma kinetics and validate chemical kinetics calculations, time resolved radical densities need to be measured. In the gas phase plasma, electrical power measurement, imaging, emission spectroscopy, laser induced fluorescence and laser scattering are typical diagnostics used to obtain key plasma properties with good accuracy. For plasmas generated in water, identical techniques as for the gas phase cannot be directly implemented and need to be modified to use.

The thesis focuses on gaining insights in detailed water vapor phase kinetics in nanosecond pulsed high density gas phase plasmas, translating these results to pure water vapor discharges and developing a stabilized plasma generation approaches in bubbles and directly in liquid to enable advanced diagnostics. For the bubble and direct liquid discharge, the thesis reports only on imaging and newly developed electrical diagnostics to enable accurate power measurements of direct discharges in liquid. All other reported diagnostics in this study were performed on gas phase water-containing discharges, including power measurement, imaging, laser induced fluorescence and Rayleigh scattering diagnostics. The detailed plasma property measurements have been performed for the low water concentration

gas phase discharge to study the plasma kinetics and validate a chemical reaction set for water vapor kinetics. The plasma kinetics for the pure vapor discharge is partially validated with previously published work [13].

1.4 Outline

In this work, the plasma water kinetics have been studied and validated by the radical density measured in a high electron density plasma filament. This enabled us to establish a validated reaction set for Ar-H_2O high density plasmas that can also be applied to pure water vapor discharges [14]. A plasma bubble reactor and plasma liquid water reactor have been developed to enable controlled studies of plasma-water interaction as well. The outline of the thesis is as follows:

- The argon water kinetics developed for low electron density plasmas from Bogaerts group [15] has been modified and extended to be used in a high electron density discharge. We validated the reaction set through comparison with H [16] and OH radical density measurements by the two-photon absorption laser induced fluorescence (TaLIF) and laser induced fluorescence (LIF) respectively in a shielded plasma jet in **Chapter 2**. The production and consumption pathways of H and OH radicals have been studied and a power and water fraction sensitivity study has also been carried out. The validated plasma kinetics is extended to use for the low electron density pure water vapor discharge for gas temperatures lower than 1000 K.
- In **Chapter 3**, the temporal and spatial OH fluorescence intensity in the same shielded plasma jet as the one used in the study of chapter 2 have been measured by LIF and studied to understand the OH radical dynamics in the high electron density gas phase discharge particularly with a focus on the spatial variation in the radial OH density profiles in and surrounding

the plasma filament. This work allows studying important aspects of radical transport leading to significant OH radical production outside the plasma filament.

- **Chapter 4** extends the reaction set described in chapter 2 to high electron density pure water kinetics with elevated gas temperatures up to 3000 K. The global model result is compared with published experimental data in [13]. A major goal of this study is to assess the difference between thermal plasma kinetics and nanosecond pulsed discharges in high specific energy as the one found in discharges in liquid water.
- A synchronized bubble-discharge system is developed to study the controlled plasma-water interaction in **Chapter 5**. Multiple discharges are generated in the same bubble and the power and emission of each discharge are measured. The underlying reason of the differences observed in multiple pulses due to memory effects in the bubble is studied and explained.
- In **Chapter 6**, a setup that enables the temporally and spatially stable discharge generation in liquid is reported. In addition, I developed voltage and current sensors to measure current and voltage waveforms with high temporal resolution enabling accurate power measurements. This new power measurement method can be adapted to accurately capture the plasma electrical characteristics and used as input for the future plasma modeling.
- A summary of the key conclusions of the study is provided in **Chapter 7**.

2 Plasma kinetics in a nanosecond pulsed filamentary discharge sustained in Ar-H_2O and H_2O*

Abstract

The plasma kinetics of Ar–H_2O and H_2O at atmospheric pressure are of interest for applications in biotechnology where rare-gas plasma jets treat liquid surfaces and in water treatment where discharges are generated in bubbles or directly in liquid water. Due to evaporation resulting from heat transfer to the liquid, for many conditions the mole fraction of water in the plasma can be large—approaching nearly pure water. In this paper, results are discussed from a combined experimental and computational investigation of the chemical kinetics in a high electron density plasma filament sustained in Ar–H_2O at atmospheric pressure. The chemical kinetics were simulated using a 0D global model, validated by measurements of the absolute OH and H densities by laser induced fluorescence (LIF) and two-photon absorption LIF. The primary sources of H and OH during the discharge pulse are dissociative excitation transfer from metastable Ar atoms and Ar dimer excimers at low water concentration and electron impact dissociation of H_2O at high water concentration. In spite of their similar sources, the density of OH was measured to be two orders of magnitude smaller than that of H at power densities on the order of 10^5 Jm^{-3}. This disparity is due to electron impact dissociation of OH during the discharge pulse and rapid reactions of OH in the

* This chapter has been published as Luo Y., Lietz A. M., Yatom S., Kushner M. J. and Bruggeman P. J. (2019) Plasma kinetics in a nanosecond pulsed filamentary discharge sustained in Ar-H_2O and H_2O, *J. Phys. D: Appl. Phys.* **52** 044003
https://doi.org/10.1088/1361-6463/aaeb14

© IOP Publishing. Reproduced with permission. All rights reserved

presence of high H and O densities in the afterglow. It is often assumed that OH is the dominant non-selective reactive species in water-containing plasmas. These results reinforce the importance of atomic species such as H and O in water containing high energy density plasmas. A numerical parametric study revealed that the lowest energy cost for H_2O_2 production is achieved at low energy densities in pure water. The high concentration of atomic radicals, which rapidly recombine, results in an overall lower energy efficiency of reactive species production. In particular, the selectivity of H_2O_2 production decreases with increasing power density which instead favors H_2 and O_2 production.

3 Temporal and spatial investigation of a nanosecond pulsed filamentary discharge sustained in Ar-H_2O using laser induced fluorescence

3.1 Introduction

The production of OH radicals in water-containing discharges enables or impacts applications in many areas, including biomedical applications [17], environmental remediation [18], surface modification [19] and plasma-assisted combustion [20]. Nanosecond pulsed discharges at atmospheric pressure often appear as filaments in these applications with a relatively high electron density of 10^{20} m^{-3} up to 10^{23} m^{-3} [10,11]. Despite the wide use of these discharges for applications, the current understanding of the plasma kinetics is still limited. Particularly the high electron density discharge kinetics is challenging due to the highly transient nature of filamentary discharges leading to fast changes in gas composition and reactive species densities. In addition, the large gradient of species densities due to the small radius of filaments (~ 100 μm) at the interface between the discharge core and surrounding gases enhances complex transport processes. Modeling such plasmas is challenging and time-resolved measurements of the 2D species density distribution is necessary to facilitate the understanding of the species production/consumption mechanism in and near the filamentary discharge. A pin-to-pin geometry can be employed to stabilize the discharges in space allowing for time and spatially resolved measurements.

Previously, experimental and simulation research of a low electron density (~10^{18} m^{-3}) He-H_2O discharge were reported in [21,22]. This low electron density glow discharge is diffuse and can be generated between electrodes with sizes of a few cm. Absorption measurements can be performed in such discharges providing accurate OH densities. The discharge can also in good approximation be modeled in 1D. A 1D model developed in [23] predicts OH and H_2O_2 density with a difference less than a factor 2 compared with the measurement of an atmospheric pressure diffuse glow discharge in He-H_2O. The model shows that electron-induced water dissociation is the dominant reaction producing the OH radical in these low electron density diffuse discharges. The OH radical reaction mechanism changes when water-containing plasma evolves from a low electron density to a high electron density. The peak OH radical density was observed in the afterglow of nanosecond pulsed discharges when the peak electron density is of the order of 10^{23} m^{-3} [24]. It suggests the importance of electron-ion recombination reactions for OH production. A more detailed high electron density kinetics of argon water plasma was reported in [16]. The time-resolved H and OH densities were measured by two-photon absorption laser-induced fluorescence (TaLIF) and laser induced fluorescence (LIF) respectively. The measured species densities were compared with a 0-D argon water kinetics model. At high specific energies in nanosecond pulsed plasmas, OH is largely dissociated by electron-induced dissociation during the pulse leading to large concentrations of H and O. In the afterglow large H and O concentrations lead to a continued OH destruction. As a result, H_2O_2 production is suppressed and H_2 and O_2 production are favored in high electron density water-containing discharges even for plasmas operating near room temperature.

The previous study focused on the kinetics in the core of the filament. In this

study, we investigated the radial diffusive transport of radicals and the OH density spatial distribution for the same nanosecond pulsed discharge as reported in chapter 2. LIF was employed to measure the temporal and spatially resolved OH density distribution. We report results for both humid and dry shielding to assess the effects of gradients in gas composition on the OH density distributions.

3.2 Experimental setup and diagnostic methods

The details of the experimental setup can be found in chapter 2. Briefly, a coaxial cylindrical tube system was used for the gas delivery. The plasma jet with shielding consists of an inner quartz tube (I.D. 1.5 mm, O.D. 3 mm) and an outer plastic tube for shielding gas to prevent the penetration of the surrounding air. The plasma jet operates at an argon flow rate of 1.34 slm (standard liter per minute) containing 0.26% H_2O. The shielding gas was either pure argon (dry shielding case, which was used in [16] and chapter 2) or an argon water mixture with the same water vapor concentration of the core flow (humid shielding case). The comparison of these two cases is used to estimate the effect of gradients in the vapor concentration on the OH production. A solid tungsten needle (diameter 1 mm) with sharp tip was placed in the center of the inner quartz tube as anode. A 200 ns high voltage pulse generated by DEI PVX-4110 pulse generator was applied to the needle electrode. The voltage amplitude and repetition rate of the pulse were fixed at 6 kV and 5 kHz respectively. A stainless-steel plate was placed 9 mm away from the tip of the quartz tube. A ballast resistor of 50 kΩ was placed between the plate electrode and the ground to limit the current (transient spark).

The power deposition into the discharge was obtained by multiplying the voltage across the discharge gap and the conduction current after correction

of the phase shift between the two probes. The voltage across the discharge was taken as the difference between the voltage measured by the high voltage probe (Tektronix P6015A) mounted at the anode and cathode side of the filament. The details of the measurement procedure can be found in chapter 2.

The OH LIF measurements were performed as in [25] and chapter 2. A four-level LIF model was used in combination with Rayleigh scattering for OH density calibration. The temporal and spatial OH density measurement was recorded at a position in the bulk of the gap, 4 mm away from the edge of the quartz tube. The gas composition at the measurement location was determined through OH fluorescence intensity quenching measurements. By changing the location of the plasma jet using a linear stage in the y direction (see Figure 3.1) perpendicular to the laser beam direction, multiple positions have been measured along the y axis. The 2D location of the discharge was determined before the start of the LIF measurement by combining an ICCD camera positioned with the lens along the y direction and a Nikon digital camera positioned with the lens along the x direction. The filament was visibly very stable, and it is assumed the discharge stayed at the same position in the y direction during the LIF measurements as supported by the LIF measurements. The discharge shown in Figure 3.1 has a diameter obtained from the visible emission of the filament of approximately 400 μm.

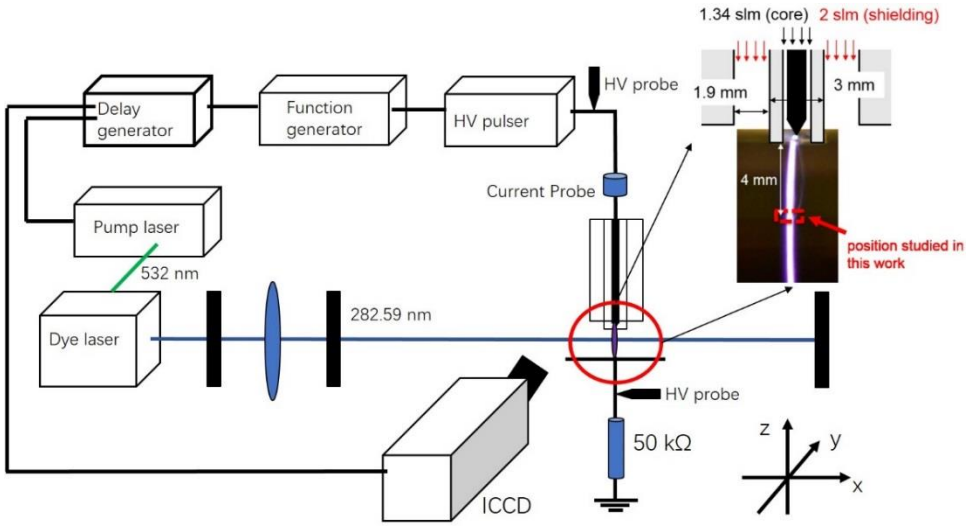

Figure 3.1 Schematic of the setup.

3.3 Model

A 0-D kinetics model identical to the one used in chapter 2 was employed in this work to understand the effect of water concentration in the shielding on the OH density in the core of the discharge. The detailed description of the model *GlobalKin* can be found in [26]. The power density and gas composition were two main input parameters to the model which were determined through power measurement and OH fluorescent intensity decay.

3.4 Results

3.4.1 Spatial gas composition distribution

The quenching time constant in the dry shielding case as shown in Figure 3.2 is determined by both water vapor and air impurity concentrations, with an inhomogeneous and unknown spatial distribution. However, the water concentration is uniform in the humid shielding and equal to 0.26%. We estimate an average air concentration that enables the estimated value to match the humid shielding contour quenching time measurement, yielding air

concentration equal to1.2%. Details can be found in chapter 2. By assuming the air concentration is the same in both dry and humid shielding cases, the water concentration in the dry shielding case was estimated. For the spatial region within 0.5 mm of the axis of symmetry, the water concentration was 0.13% and the region beyond 1 mm, the water concentration is approximately 0.025%. The transition from the high-water concentration to low-water concentration and from the low quenching time to high quenching time in the dry shielding case both occurred at a radial distance of approximately 1 mm away from the axis of the symmetry. Since the nozzle has I.D. 1.5 mm and O.D. 3mm, this transition zone is between the water-containing core flow (0.26% water vapor) and dry shielding flow (0% water vapor). The discharge was located within 0.5 mm away from the axis of symmetry in the experiment.

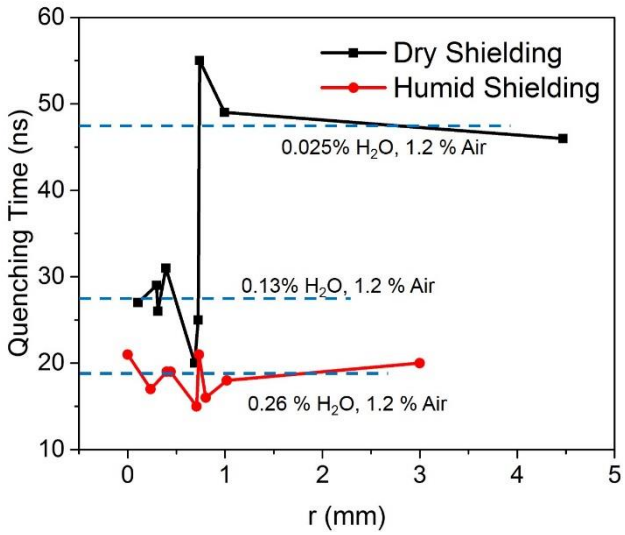

Figure 3.2 The OH fluorescence intensity quenching time against radial distance to the center of the nozzle (axis of symmetry) in the dry shielding and the humid shielding cases.

3.4.2 Power

Voltage and current waveforms measured in the experiment for both humid

and dry shielding cases are shown in Figure 3.3. The applied voltage was kept constant at 6 kV. The conduction current of the humid shielding case reduced by almost 10% compared with the dry shielding case and the voltage in the humid shielding drops earlier due to this faster increase of the conduction current. As a result, the power deposition into the dry shielding jet is 10% larger than the power deposited into the humid shielding jet. Similar phenomenon has been observed in [27], with increasing water concentration the input power of sinusoidal voltage driven Ar-H_2O jet decreases. This can be attributed to the increased water concentration coinciding with an increase in electron attachment and increased electron energy losses in vibrational excitation.

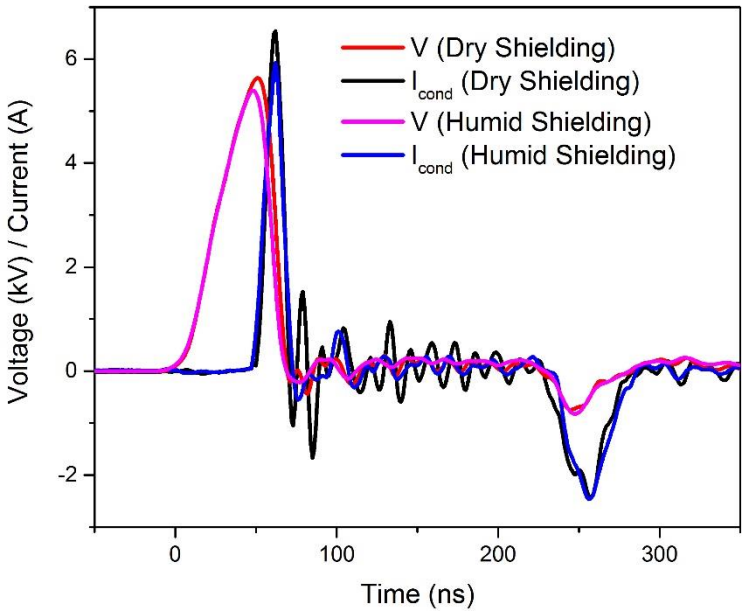

Figure 3.3 Voltage and conduction current waveform for the dry and humid shielding case.

3.4.3 Time-resolved absolute OH density

The time-resolved ground state absolute OH density in the core of the discharge filament as obtained by OH LIF for both the dry and humid shielding case are shown in Figure 3.4. The OH density in the humid shielding case is twice the OH density in the dry shielding case, which is mainly due to the factor

2 difference in the water concentration at the position of the discharge filament (see Figure 3.2). The electron-induced water dissociation (R3.1) and the electron-induced OH dissociation (R3.2) are the dominant OH production and consumption reactions respectively during the discharge as reported in chapter 2.

$$e^- + H_2O \rightarrow e^- + H + OH \qquad (R3.1)$$

$$e^- + OH \rightarrow e^- + H + O \qquad (R3.2)$$

Assuming a quasi-steady state of the OH radical, which means the production and consumption of the OH radical is approximately the same. The relation between the OH density (n_{OH}) and H_2O density (n_{H_2O}) is established in (3.1). k_1 and k_2 are the reaction rate coefficient of reactions R3.1 and R3.2, respectively. The energy deposition difference in the dry shielding and humid shielding cases is only 10%. The electron density and electron temperature, according to the model, are very similar for both cases. The peak electron temperature of 4 to 5 eV was obtained. As a result, the ratio of reaction rate coefficient k_1 and k_2 is in good approximation to be the same for both dry and humid case. When the ratio k_1/k_2 is constant, (3.1) leads to a proportional increase of the OH density with the water density during the discharge.

$$n_{OH} = n_{H_2O}\frac{k_1}{k_2} \qquad (3.1)$$

In the afterglow, the dominant OH production is due to reaction (R3.3) and the dominant OH consumption is due to reaction (R3.4) as described in chapter 2. The model shows that the increase in water concentration for the humid shielding case leads to an increase in H, OH and O densities. Higher H density leads to an increase in OH production (reaction (R3.3)). As a result, the OH

density in the afterglow of the humid shielding case remains 2 times larger than the OH density in the afterglow of the dry shielding case.

$$H + O + Ar \rightarrow OH + Ar \qquad (R3.3)$$

$$OH + O \rightarrow H + O_2 \qquad (R3.4)$$

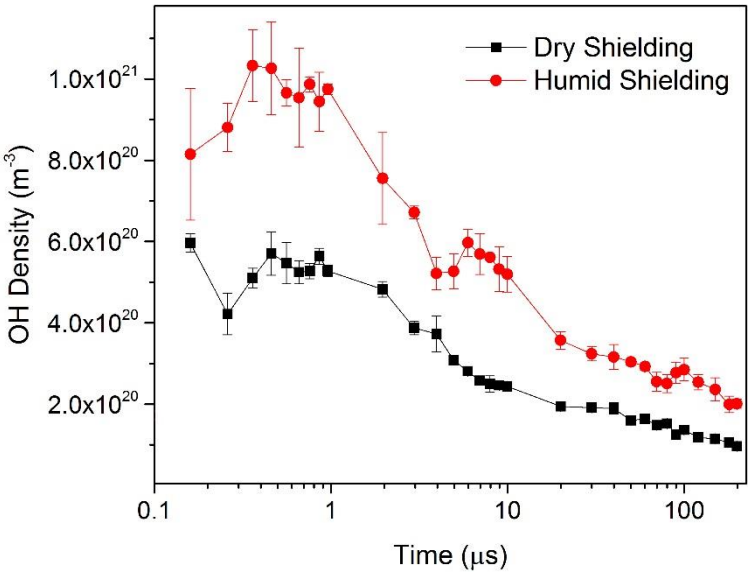

Figure 3.4 Absolute OH density in the dry shielding and humid shielding case.

3.4.4 Spatial OH LIF intensity contour

The OH fluorescence intensity contours at an axial position of 4 mm from the nozzle of the dry and humid shielding case at 5 μs and 100 μs after the discharge pulse are shown in Figure 3.5. In both cases, the filament position is at one side of the tube most likely due to water concentration gradients and a possible imperfect alignment of the needle compared to the quartz tube. The local minimum in the OH fluorescence contour corresponds to the position of the discharge core. The recorded quenching times in the 100 μs contour of the dry and humid shielding case at 9 different positions labeled in Figure 3.5(b) and (d) respectively, are provided in Table 3.1. In the dry shielding case, the

average quenching time at positions corresponding to the low fluorescence intensity zone is higher than the average quenching time at positions corresponding to the high fluorescence intensity zone with a maximum difference of approximately 30%. In the humid shielding case, the quenching time difference is smaller because the quenching time is mainly determined by the H_2O density which is the same in the core and the shielding gas flows. The gas temperature differences in the afterglow in both cases are at most 100 K leading to a difference in OH density by a change in Boltzmann factor of at most 20%. The OH fluorescence intensities can have in both cases a factor 2 difference. The differences in the OH fluorescence intensities represent the differences in the OH absolute density. The relative changes in the OH fluorescence intensity 2D contour is thus representative of the relative changes in the OH density at different spatial locations in and around the core of the discharge.

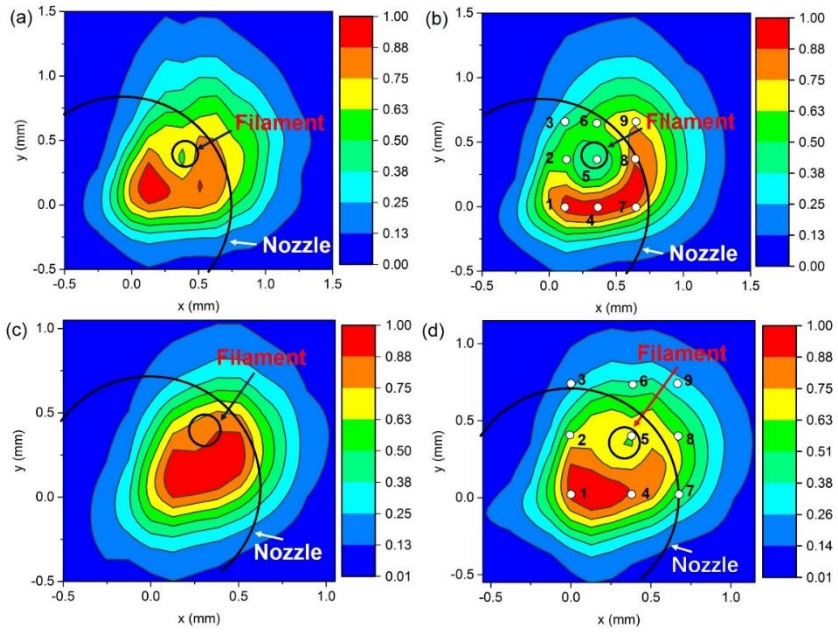

Figure 3.5 Normalized OH fluorescence intensity of (a) the dry shielding case at 5 μs and (b) the dry shielding case at 100 μs (c) the humid shielding case at 5 μs and (d) the humid shielding case at 100 μs

Table 3.1 The quenching time at multiple positions in the dry and humid shielding case.

Point	Dry Shielding (ns)	Humid Shielding (ns)
1	27	21
2	26	17
3	20	15
4	29	19
5	31	19
6	25	16
7	55	21
8	46	20
9	49	18

The position numbers correspond to the numbers in Figure 3.5. The positions in dry shielding are not necessary the same as in the humid shielding by labels.

In Figure 3.6, the radical distribution of the relative OH fluorescence intensity is shown from 1 μs to 100 μs for the dry shielding (a) and humid shielding case (b). As time evolves, the OH fluorescent intensity decreases. At 1 μs, the radial distribution has only one peak. A local minimum of the OH fluorescence intensity appears at 2 μs and becomes even more pronounced at 100 μs. This local minimum in the radial distribution of OH fluorescence intensity in the late afterglow is the result of the faster recombination of the OH density in the plasma core than in the immediate surroundings of the filament. The decay of the OH density in the core of the discharge is mainly due to the reaction between OH and O radical (R3) in the afterglow as reported in chapter 2. An important question is whether the increased effective OH lifetime outside the

core plasma is due to an increased production of OH in the surrounding of the core discharge particularly as the OH density in the core is lower than the surrounding of the filament. Assuming the OH radical is mainly consumed by the recombination of OH with OH and Ar as third body, this underestimation yields an OH lifetime less than 5 μs. It suggests that OH production in the surrounding region of the discharge core is needed to sustain the OH density. Transport of OH, as shown in Figure 3.6, is not possible since the OH density is lower in the core than the surroundings. The proposed mechanism is based on H and O, the dominant radicals in the core of the filament, diffuse from the core to the surrounding of the discharge. The diffusion time of the H is in the order of 50 μs which aligns with the time scale of the local minimal formation in the radical OH profile shown in Figure 3.6. The dominant production mechanism of the OH radical outside the plasma region is most likely the recombination of the H and O radical by reaction (R3), which is also the dominant production mechanism of OH in the core of the discharge as shown in chapter 2. Considering that the H and O densities are two orders of magnitude higher than the OH density in the core plasma discharge and the diffusion coefficient of H is one order of magnitude higher than the diffusion coefficients of OH and O, diffusive transportation of the H and O radicals is sufficient to provide large enough densities of the reactants in reaction (R3.3) to yield a considerable OH density production in spite the H density in the core drops at approximately 50 μs in the afterglow. This proposed mechanism is very different than the mechanism proposed based on charge exchange and dissociative recombination explaining the hollow profile during the active plasma phased [39].

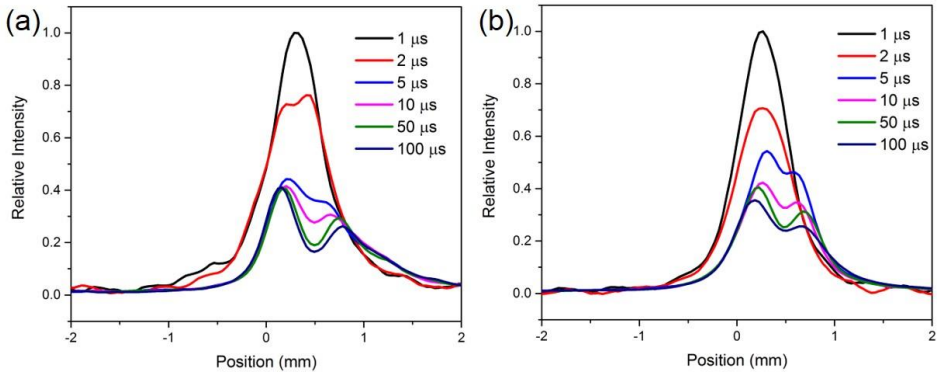

Figure 3.6 Radial distribution of the OH fluorescence intensity at different times in the afterglow for (a) the dry shielding and (b) the humid shielding case

3.5 Conclusion

In this study, spatial OH fluorescence intensity has been reported for both dry and humid shielding cases. A local minimum in the OH density is observed in the afterglow from 5 μs in the afterglow at the position of the filament. The effective decay time of OH in the surrounding of the discharge core is at least a factor 2 higher than observed lifetime of OH which indicates production of OH in the surrounding of the filament. The proposed mechanism is that H and O diffusion from the core leading to OH formation in the surrounding of the core discharge. This mechanism is different from the one previously reported based on ionic reaction occurring on a much shorter time scale and compatible with large OH density surrounding the plasma filament during the ionizing plasma phase.

4 Plasma kinetics study of high electron density nanosecond pulsed filamentary discharge in water vapor

4.1 Introduction

The study of water-containing discharges have been driven by the wide range of applications from environmental remediation and wound healing to nanomaterial synthesis and plasma assisted combustion [10]. Although many different applications have been extensively studied in the plasma community, the kinetics underpinning the plasma processes are not well known for the high electron density (10^{22} ~ 10^{23} m^{-3}) discharges in water vapor. The kinetics of the high electron density nanosecond pulsed discharge sustained in Ar-H_2O mixtures has been studied with a 0-D kinetics model and compared with species density measurements by laser diagnostics, shown in chapter 2. The reaction set used in that study is not suitable for gas temperatures higher than 1000 K which are commonly found in high electron density nanosecond water discharges. Several dominant reactions at elevated gas temperatures were not included in the reaction set that was developed for relatively low gas temperatures. These include thermal dissociation reactions that can be important at elevated gas temperature in high electron density water vapor plasmas.

Plasmas generated in pure water previously studied include thermal plasmas [28], microsecond [29] and nanosecond pulsed non-equilibrium discharges [30]. These discharges have been characterized using electrical measurements, imaging and spectroscopy [10]. Mededovic and Locke studied

the kinetics of a microsecond pulsed discharge in water [31]. Their model defined two main areas of the discharge: a discharge core and a recombination zone with different chemical reactions. Although the model did not consider electron- and ion-induced reactions, it showed a good agreement with the long-lived species densities measured in the liquid phase. The predicted gas temperature from the model reached a maximum of 5000 K suggesting indeed that thermally induced reactions might play a key role in radical production.

Sainct et al [13,32,33] experimentally studied nanosecond non-equilibrium discharges in pure water vapor by imaging, emission spectroscopy, laser induced fluorescence and gas chromatography. The time resolved gas temperature and OH fluorescence intensity, together with the density of end products (H_2 and O_2) were reported. The measured electron density was of the order of 10^{22} m^{-3} using H Balmer lines (H_α and H_β) and the measured peak gas temperature was approximately 1600 K using PLIF. The experiment showed that mainly H_2 and O_2 were produced and the produced H_2O_2 was below the detection limit at the end of the power cycle.

In this chapter, we extend the reaction set from chapter 2 to conditions with gas temperatures up to 3000 K as found in pure water vapor nanosecond pulsed discharges. The modified kinetics was implemented in the 0-D model *GlobalKin* [26] and the results were compared with the experiments performed on repetitively pulsed nanosecond pulsed discharges in pure water vapor by Sainct et al [13,33].

The key research questions to be addressed in this work are:

1) What modifications and additions to the reaction set reported in chapter 2 are required to make it suitable to model high electron density pure water vapor

discharges?

2) What is the dominant radical composition in the afterglow and how is it different from the low water concentration high electron density discharges?

3) What is the difference in the long-lived species produced by a high electron density non-equilibrium nanosecond pulsed discharge and by a recombining thermal plasma?

4.2 Experimental conditions and computational methods

4.2.1 Experimental conditions

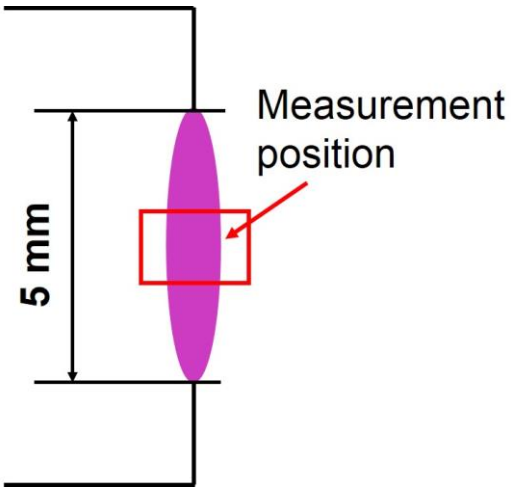

Figure 4.1 Schematic of the nanosecond water vapor discharge. The data measured at the center was used for model validation.

The plasma condition investigated in this work is a nanosecond repetitive pulsed spark discharge (NRP-Spark) in pure water vapor at an initial gas temperature of 475 K and atmospheric pressure as reported by Sainct et al [13]. A detailed description of the experimental setup can be found in [13] and the schematic is shown in Figure 4.1. The water vapor was fed in parallel with the discharge axial direction (vertical direction) and with an average speed of 0.13 m/s. The plasma discharge was generated in a pin-to-pin geometry with

a gap of 5 mm. Voltage pulses with a 20 ns duration, at 10 kHz pulse repetition frequency and amplitude up to 30 kV were applied across the electrodes. The electron density and gas temperature used to compare with the model were measured in the center of the discharge gap.

4.2.2 0-D kinetics model

A 0-D model *Globalkin* [26] has been used in this study and is identical to the model used in chapter 2. *Globalkin* contains a Boltzmann solver to calculate the electron energy distribution function (EEDF) for a given gas composition and for a range of reduced electric fields. Since in the high electron density water vapor plasma the gas composition can change significantly during the discharge, the EEDF was set to be updated every 1 ns during the discharge pulse. Then the EEDF was further used to calculate the electron transport coefficients and electron impact reaction rate coefficients. The mean electron energy and gas temperature were obtained from the electron energy equation and the energy equation and updated at every time step of the simulation.

Globalkin is able to calculate the plasma composition as a function of time at either constant volume or constant pressure. A two-stage calculation procedure was employed in the simulation as a simplified model to consider the pressure variation due to fast gas heating and shock wave relaxation. The first stage of the calculation was performed at a constant volume and allowed for pressure build-up. The second stage of the calculation corresponding to the afterglow plasma after pressure relaxation due to shock wave release was performed at a constant pressure of 1 atm. The initial conditions of the second stage were calculated assuming a shock wave relaxation process including the change of pressure, gas temperature and the absolute number density of the total gas mixture. We manually reduced the after-shock pressure to

atmospheric pressure and calculated the corresponding after-shock gas temperature to accommodate for the internal energy loss due to shock wave release. The detailed procedure of the after-shock temperature calculation can be seen in Appendix 1. The number density of the gas mixture after the shock wave relaxation was determined by applying the ideal gas law for the after-shock pressure and gas temperature.

The gas temperature and pressure drop (due to the shock wave relaxation) in the model was assumed to be instantaneously fast to occur at the time corresponding to the beginning or the end of the expected physical pressure relaxation process. Hence, no chemical reactions were considered during the shock wave relaxation. The time corresponding to the beginning of the shock wave relaxation process (t_1) was chosen based on the following procedure. First, the constant volume calculation given the experimental condition was run for the whole power cycle. At this point, the gas composition and the gas temperature at the maximum gas temperature time were taken to calculate the shock wave pressure relaxation time. The derivation of the shock wave pressure relaxation time is provided in Appendix 2. Then, the shock wave pressure relaxation time calculated in the previous step was multiplied by a factor of 0.9 to ensure the value obtained was within the pressure relaxation time for the highest gas temperature. The pressure relaxation time (t_{relax}) at the beginning of the shock wave relaxation process (t_1) was calculated following the same method mentioned in the previous steps and used to calculate the time corresponding to the end of the shock wave relaxation process t_2 ($t_2 = t_1 + t_{relax}$). Under the experimental condition, t_1 = 40.6 ns and t_2 = 94.6 ns. It was confirmed that the number densities of the long-lived species, such as H_2, O_2 and H_2O_2, at the end of the power cycle are not sensitive to the time when the instantaneous shock wave relaxation is assumed. For the simulations, the

instantaneous shock wave relaxation was set at 94.6 ns and defined it as the cutoff time separating the constant volume and constant pressure calculation. A schematic representation of the simulation procedure is shown in Figure 4.2.

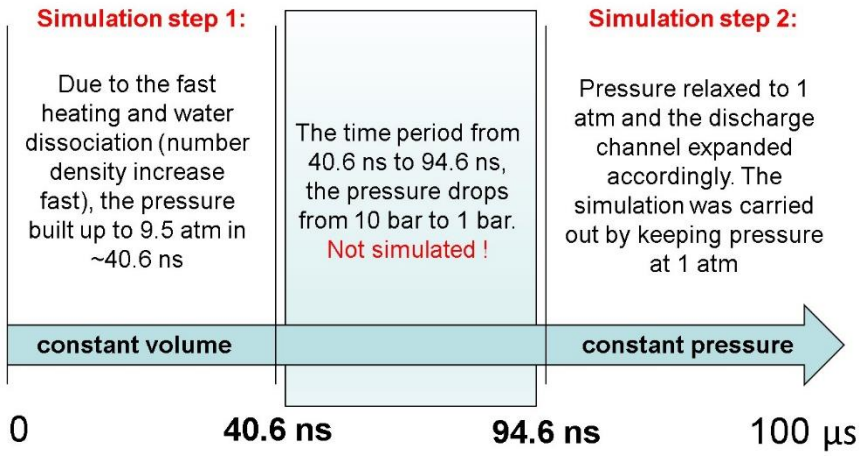

Figure 4.2 Schematic representation of the plasma kinetics modeling procedure used.

The reaction set used in chapter 2 has been complemented and adapted to enable calculations for gas temperatures above 1000 K through updating the reaction rate coefficients so they remain valid at higher gas temperatures and adding thermal dissociation reactions which are negligible at the lower gas temperatures. The changes to the reaction set consist of:

(1) The excited species OH*, H* and O* were not included self-consistently for all excitations and de-excitation process in reaction set used in chapter 2 since several of the reaction rate coefficients are not well known. We excluded these reactions as several of these reactions led to unrealistic high temperatures (> 1000 K) at higher power densities.

(2) The reaction rates of the dominant reactions for H, OH and O have been updated to be consistent with reported values for gas temperatures up to 3000 K. The updated reaction rate coefficients are shown in Table 4.1.

(3) Thermal dissociation reactions for OH, H_2, O_2 and H_2O have been added and are also listed in Table 4.1.

In this simulation, the measured electron density in the experiment was fitted by adjusting the experimentally obtained power waveform (see further). The radial thermal boundary of the simulation zone was set as 475 K which was equal to the background water vapor temperature and only thermal conduction was considered. The number density of long-lived species, such as H_2 and O_2, measured at the outlet of the plasma reactor were used to assess the capability of the reaction set and model to predict the dominant plasma kinetics in the late afterglow. Since the experiment was performed at a repetition rate of 10 kHz and the gas flow velocity was 0.13 cm/s, the gas residence time in the plasma is approximately 2 seconds which is four orders of magnitude higher than the period of the power cycle (100 μs). The flow effect on the kinetics during the power cycle is thus negligible. The differences of the calculated long-lived species densities by a single voltage pulse and by two consecutive pulses is less than 5%. This is because of the high dissociation degree of molecules at high power densities. H_2 and O_2 remaining from the previous pulse are dissociated into H and O which have one order of magnitude lower number densities compared with the H and O which are produced from the fresh H_2O in the current pulse. Hence, the presented chapter shows single pulse calculations.

Table 4.1 The updated reactions in the reaction set chapter 2

Reaction	A	B	C	T range (K)	Ref
$OH + O \rightarrow H + O_2$	4.55×10^{-12}	0.40	-371.6	250-5000	[34]
$H + HO_2 \rightarrow OH + OH$	5.50×10^{-11}	0.88	-32.47	200-3000	[34]
$OH + OH + H_2O \rightarrow H_2O_2 + H_2O$	1.01×10^{-30}	-4.30	-340.370	300-3000	[34]
$H + OH + H_2O \rightarrow H_2O + H_2O$	4.16×10^{-31}	-1.18	251.37	300-3000	[34]
$H + OH + H_2 \rightarrow H_2O + H_2$	8.32×10^{-32}	-1.18	251.37	300-3000	[34,35]
$H + OH + O_2 \rightarrow H_2O + O_2$	1.14×10^{-31}	-1.18	251.37	300-3000	[34,35]
$H_2 + O \rightarrow OH + H$	3.07×10^{-13}	2.7	3150.0	297-3530	[34]
$H + H + H_2 \rightarrow H_2 + H_2$	8.82×10^{-33}	0	0.0	50-5000	[34]
$H + H + H_2O \rightarrow H_2 + H_2O$	8.82×10^{-33}	0	0.0	50-5000	[34]
$H + H + H_2O(v) \rightarrow H_2 + H_2O(v)$	8.82×10^{-33}	0	0.0	50-5000	[34]
$H + H + O_3 \rightarrow H_2 + O_3$	8.82×10^{-33}	0	0.0	50-5000	[34]
$H + H + O_2 \rightarrow H_2 + O_2$	8.82×10^{-33}	0	0.0	50-5000	[34]
$H_2O + M \rightarrow H + OH + M$	8.82×10^{-8}	0	58489.0	300-3000	[35]
$OH + M \rightarrow H + O + M$	4.69×10^{-8}	0	50590.0	300-3000	[35]
$H_2 + M \rightarrow H + H + M$	2.10×10^{-9}	0	51573.0	300-3000	[35]
$O_2 + M \rightarrow O + O + M$	1.72×10^{-9}	0	58969.0	300-3000	[35]

The reaction rates shown in Table 4.1 are in Arrhenius form, which can be represented as $k = A(T_g/300)^B \exp(-C/T_g)$. The unit of A is either s^{-1}, $cm^3\ s^{-1}$ or $cm^6\ s^{-1}$ for the first, second and third order reactions respectively. The coefficient B is nondimensional. The unit of C is K.

In chapter 2, the water vapor kinetics has only been studied for energy deposition values up to 0.05 eV/molecule due to the limit validity of the reaction set at higher gas temperature. In this study the specific energy has been extended to 1.22 eV/molecule (corresponding to 1.9 mJ – the experimental

condition) to obtain more insights about the effect of energy deposition and corresponding gas heating on the species production in the plasma. The dominant radicals and long-lived species densities were studied under a range of specific energy (from 0.00 5 to 1.22 eV/molecule) bridging the low energy deposition conditions in chapter 2 and the current experimental condition. Two sets of thermal conductivities were employed, including a temperature-dependent material thermal conductivity of the gas mixture and an enhanced effective thermal conductivity (3 W/m-K) of the gas mixture. It has been shown in chapter 2 that in the lower energy deposition and lower gas temperature water-containing plasma, the temperature dependent material thermal conductivity is a good approximation of the total heat transfer effect. However this is not the case for the current experimental condition in which an enhanced thermal conductivity is used to account for conductive and radiative heat loss in the experiment (see further).

4.3 Model validation

4.3.1 Power deposition and electron density

The power deposition into the discharge was obtained by multiplying the measured voltage and current waveform [13]. The energy per pulse was obtained by integrating the obtained power waveform. Two modifications to the original experimental power waveform were investigated as shown in Figure 4.3. The spikes and oscillations in the experimental power waveform after 30 ns were neglected (P_1). This reduced the energy deposition by 4.2% compared to the experimental value. As the experimental power waveform is less accurate in the region (after 30 ns) due to oscillations induced by inductance effects but some additional power dissipation will be present in the afterglow, a second modification is used as the input to the model by adding a tail to the

first modification after 30 ns (P_2) which leads to 13% more energy deposition in the afterglow and a better match with the electron density decay measured in the experiment. (see further)

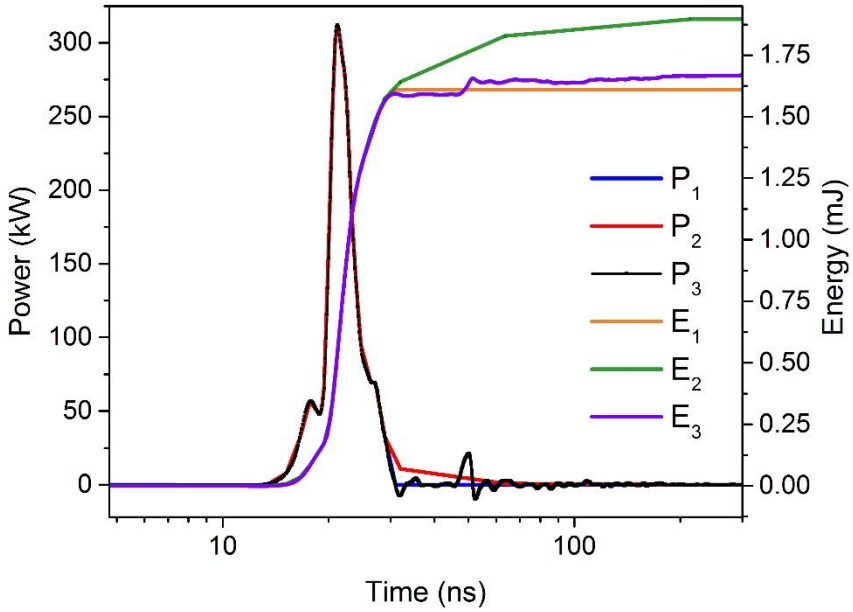

Figure 4.3 Comparison of the measured power and energy waveform in the experiment (P_3, E_3) and the two power (P_1 and P_2) and energy waveforms (E_1 and E_2) used for the plasma kinetics model. P_1 and E_1 represent the power and energy waveform neglecting experimental power deposition after 30 ns, P_2 and E_2 represent the power and energy waveform with an artificial linear decrease in power after 30 ns.

The plasma volume was calculated by treating the plasma as a cylinder with a diameter of 200 µm (the diameter of the anode is 200 µm and is equal to the measured width of the emission during the voltage pulse) and a length of 5 mm. The corresponding power density was used as the input parameter of the plasma kinetics model, which was obtained by dividing the power waveform with the plasma volume. The electron densities obtained from power waveform P_1 and P_2 are shown in Figure 4.4 together with the measured electron density

measured by Stark broadening neglecting any other broadening mechanisms. The FWHM due to Stark broadening for H_β at the peak electron density is 3.6 nm which is one order of magnitude higher than the van der Waals FWHM at a gas temperature of 2083 K and pressure of 9.5 atm at 40.6 ns. The FWHM of the Stark broadening of H_α is only a factor 3 larger than the van der Waals FWHM under the same conditions. Therefore, the electron density deduced from H_α might be an overestimation and the n_e obtained from H_β line is preferred for the model results comparison. The electron density obtained with power waveform P_2 with the additional power in the afterglow shows better agreement with the experimental result than the electron density obtained with power waveform P_1. Therefore, power waveform P_2 was used as the input parameter for the model to obtain all remaining results in this chapter.

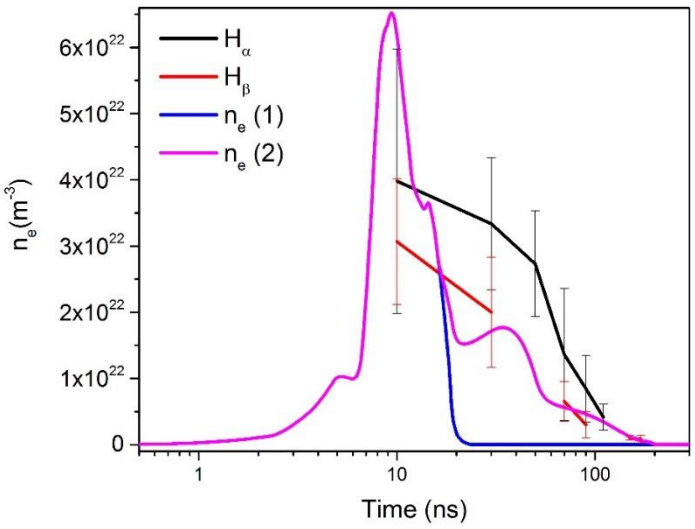

Figure 4.4 Comparison of the electron density measured in the experiment and obtained from the model using a constant volume calculation, "n_e (1)" corresponds to the calculation with power waveform P_1 and "n_e (2)" corresponds to the calculation with power waveform P_2

4.3.2 Gas temperature

As the two-stage procedure was adapted in this work, we firstly examine the gas temperature during the constant volume calculation and then study the gas temperature during the constant pressure calculation. The temperature drop due to the shock wave release is considered.

The outcomes of a constant volume calculation are shown in Figure 4.5. The gas temperature increases from 475 K to approximate 1500 K within 10 ns due to fast heating which is the result of chemical reaction enthalpy release in radical/ion recombination and ion charge exchange reactions. The three-body recombination between H and OH radicals in the presence of water (R4.1) and the hydration reaction of O_2^+ (R4.2) account for approximately 50 % of the gas heating. During the constant volume calculation, the heating time scale is shorter than the pressure relaxation time and no radial expansion of the plasma channel needs to be considered, motivating the constant volume approach.

$$H + OH + H_2O \rightarrow H_2O + H_2O \qquad \text{(R4.1)}$$

$$O_2^+ + H_2O \rightarrow H_2O_3^+ \qquad \text{(R4.2)}$$

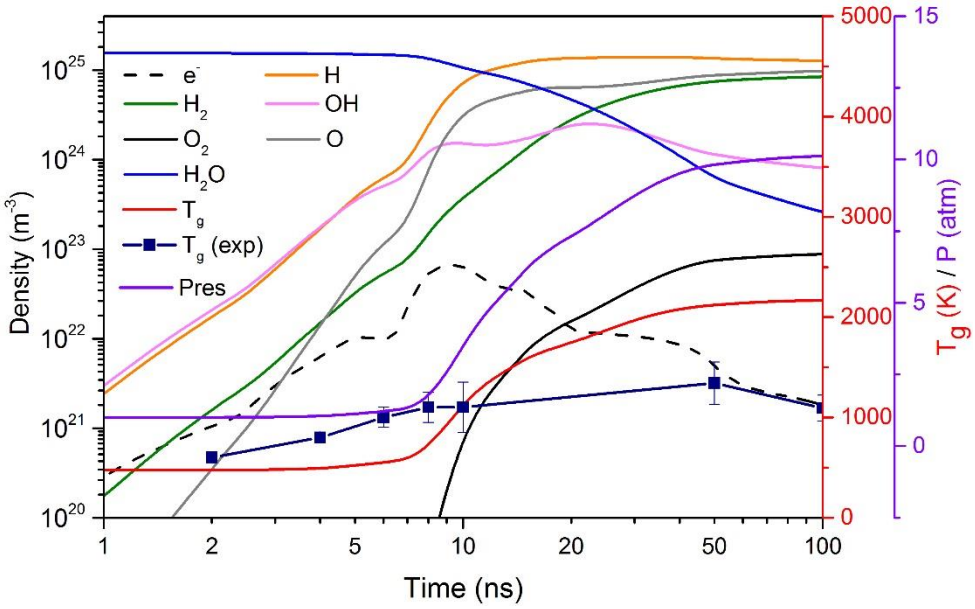

Figure 4.5 Selected species concentrations obtained with a constant volume calculation. The calculated pressure and gas temperature are also provided. The experimental gas temperature is shown as comparison.

The initial gas composition of the constant pressure calculation was chosen as the same gas composition of constant volume calculation at 2167 K, the temperature at the cutoff time. The initial gas temperature of the constant pressure calculation was set to be 1607 K after correcting for the shock wave release.(see Appendix 1)

The comparison between the measured gas temperature by OES of the N_2(C-B) transition and OH laser induced fluorescence (LIF) and the simulation is shown in Figure 4.6. The use of the enhanced effective thermal conductivity of 3 W/m-K enables the gas temperature to drop to 475 K at 100 μs. The gas temperature predicted by the model matches well with the one measured in the experiment in the afterglow (t > 0.2 μs). The measured gas temperature in the afterglow by OH LIF is a spatially averaged measurement over the area of OH radicals which is larger than the plasma filament. This might lead to an

underestimate of the actual gas temperature at the filament position, particularly in the early afterglow. During the discharge-on period, the model underestimates the gas temperature up to 8 ns. The underestimation of the gas temperature at such a short time scale is most likely due to transient ionization wave effects that cannot be captured in a 0-D model.

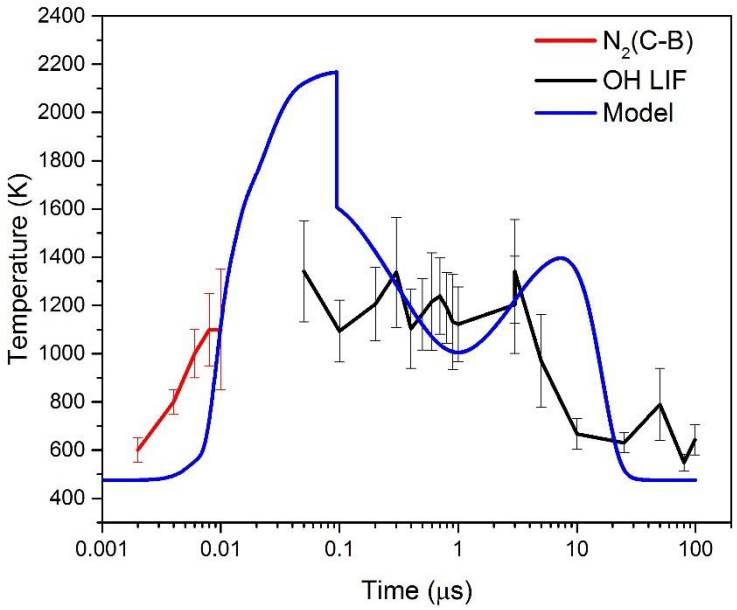

Figure 4.6 The comparison of the measured and calculated gas temperature.

4.3.3 Afterglow chemistry and H_2-O_2 production

The discharge leads to a large amount of dissociation of H_2O with O, H and OH as dominant radicals. The recombination of these radicals leads to the formation of H_2, O_2 and H_2O_2. The experiment found a ratio of H_2 and O_2 density equal to 2. The H_2O_2 concentration was formed to be below the detection limit. [33] The simulation results in Figure 4.7 show that the density of H_2 is also twice the O_2 density and the H_2O_2 has a number density two order of magnitude lower than the density of H_2 and O_2, consistent with the measurements. The experimentally reported energy efficiency for H_2

production is approximately 0.8 g/kWh. [33] In the simulation, 1.9 mJ was applied to the water vapor and 7% of the water vapor has been converted to H_2 at the end of the pulse. This leads to a calculated H_2 production energy efficiency of approximately 1 g/kWh, which is in excellent agreement with the experiment. Nonetheless, the H_2 and O_2 density in the afterglow are strongly impacted by the gas temperature, as will be discussed in the next section.

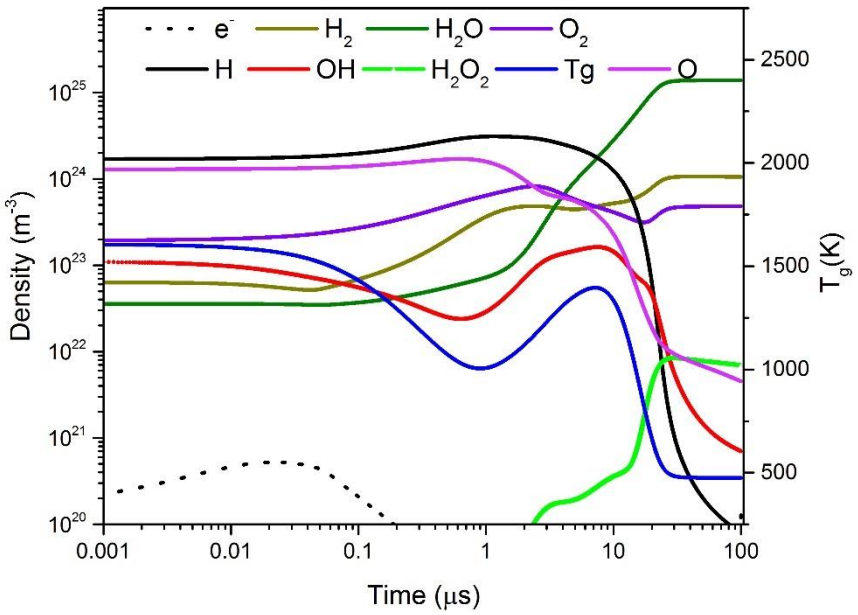

Figure 4.7 Time-resolved species densities in the afterglow (constant pressure calculation).

4.4 Power Dependence

In the reported experimental conditions by Sainct et al [13] the electron density was found to be of the order of 10^{22} m^{-3}. The H_2 and O_2 densities are two order of magnitude higher than the density of H_2O_2 100 μs after the pulse in the simulation. This is consistent with the calculations performed in chapter 2 showing the energy efficiency of the H_2O_2 production in pure water vapor discharges increased with a decrease of energy density/electron density in a much lower range of energy deposition compared with the current

experimental condition.

Figure 4.8 shows the dominant radicals and molecules at the end of the constant volume calculation (t = 94.6 ns) and long-lived species at the end of the constant pressure calculation (t = 100 μs) using both temperature-dependent calculated thermal conductivity and enhanced effective thermal conductivity (set as 3 W/m-K). When the power density deposition is at 0.005 eV/molecule, the H and OH densities are the same and significantly larger than the O density. As the electron density increases due to the increase of power density, OH radicals become increasingly dissociated by electrons. The O radical density becomes larger than the OH radical density at 0.75 eV/molecule. This transition occurs at an energy deposition at which the OH density reaches its maximum i.e. the production of OH is in quasi-equilibrium with the OH consumption during the voltage pulse. The dominant OH production reaction for this condition is water dissociation by electron impact and dissociation reactions of water with H and O radicals as shown in R4.5, R4.6 and R4.7.

$$e^- + H_2O \rightarrow e^- + H + OH \qquad \text{(R4.5)}$$

$$H_2O + H \rightarrow H_2 + OH \qquad \text{(R4.6)}$$

$$H_2O + O \rightarrow OH + OH \qquad \text{(R4.7)}$$

In the high electron density cases ($n_e \sim 10^{22}$ m^{-3}), more than 90% of the water is dissociated, the H and O are the two dominant species in the plasma, present at significantly higher densities than the electron density. This is different than for the Ar + 0.1% H_2O case reported in chapter 2 in which the electron density remains higher than the H and OH densities in the first 20 ns for higher power densities. The dominant consumption of the OH radical

remains to be electron-induced dissociation (R4.8) during the discharge which is also the dominant production reaction for H and O radicals.

$$e^- + OH \rightarrow e^- + H + O \qquad \text{(R4.8)}$$

The H_2 and O_2 density in the afterglow are determined by both the production of H and O densities in the constant volume process and strongly impacted by the gas temperature via thermal dissociation. Both the production and the consumption of H_2 and O_2 increase with the increased gas temperature. This leads to a maximum at 0.2 eV/molecule for H_2 and O_2 densities as shown in Figure 8(b) in the case of the thermal dependent thermal conductivity and a maximum at 0.4 eV/molecule for H_2 and O_2 densities as shown in Figure 8(d) in the case of the enhanced effective thermal conductivity. This more effective thermal conductivity reduces the gas temperature more quickly in the afterglow leading to a more effective H_2 and O_2 production. The differences observed in the number densities of H_2 and O_2 in 8(b) and 8(d) can be an order of magnitude and the differences observed in the number densities of H_2O_2 in 8(b) and 8(d) can be even larger. H_2O_2 is produced by reaction R4.9 and the reaction rate is larger at lower gas temperatures.

$$OH + OH + M \rightarrow H_2O_2 + M \qquad \text{(R4.9)}$$

in which M = H_2, O_2, H_2O. In addition, the 3 body recombination of OH with H_2 and O_2 as third body has at least one order of magnitude lower rate coefficient than with H_2O given the gas temperature measured in the experiment.

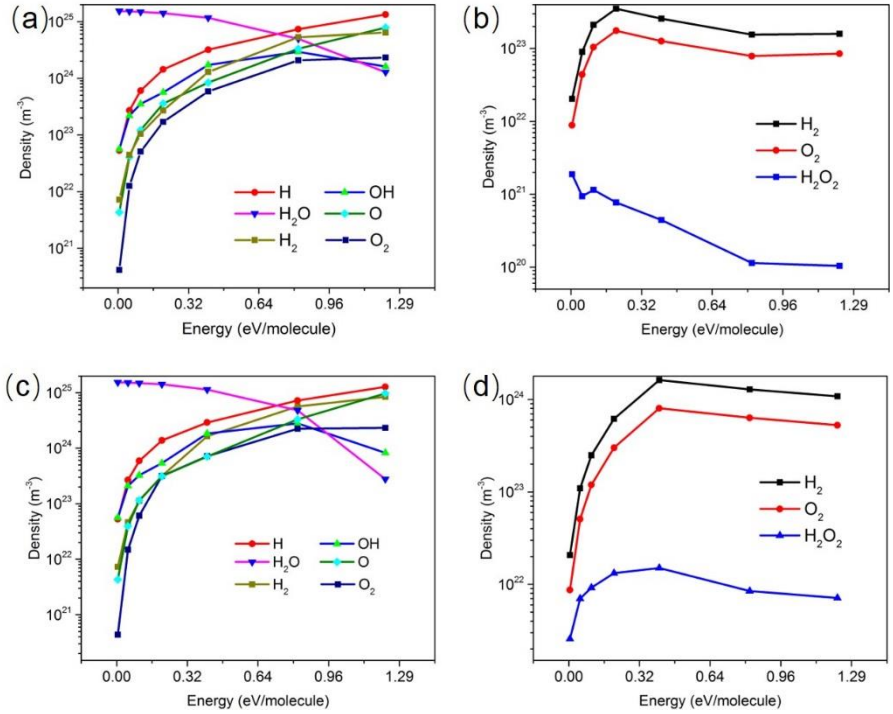

Figure 4.8 The dominant radicals and molecules densities at the end of the constant volume calculation (t = 94.6 ns) and at the end of the constant pressure calculation (t = 100 μs) when calculated using a temperature dependent thermal conductivity are shown in (a) and (b) and when calculated using an enhanced effective thermal conductivity 3 W/m-K are shown in (c) and (d).

4.5 Nanosecond high specific energy discharge vs thermal equilibrium

A high specific energy nanosecond pulsed discharge in water vapor can reach a gas temperature as high as 2167 K. What are the differences between the H_2, O_2 and H_2O_2 production by a nanosecond pulsed discharge with a high specific energy and thermal dissociation plasma at elevated temperature? In order to estimate the effect of thermal dissociation, a thermal equilibrium water vapor gas composition was assumed at the beginning of the constant pressure calculation at a gas temperature of 3000 K. The main species densities as a

function of time, calculated with the same thermal boundary conditions as for the nanosecond pulsed plasma are shown in Figure 4.9. The initial gas composition of the nanosecond pulsed discharge for the constant pressure calculation and the thermal equilibrium composition of H_2O at 3000K is shown in Table 4.2.

Table 4.2 Initial species mole fraction: comparison between nanosecond pulsed discharge and thermal plasma

Species Name	Initial composition of nanosecond pulsed discharge	Thermal equilibrium composition at 3000 K
H	3.72e-1	5.76e-2
H_2	2.45e-1	1.35e-1
O	2.84e-1	2.41e-2
OH	2.41e-2	9.36e-2
H_2O	8.10e-3	6.44e-1
O_2	6.75e-2	4.63e-2
HO_2	5.30e-6	3.79e-5
H_2O_2	9.96e-6	3.79e-5

Note that the mole fractions of H and O are lower in the equilibrium composition at 3000 K compared with the nanosecond pulsed discharge and OH remains a dominant radical for equilibrium composition at 3000 K.

Figure 4.9 shows that at 100 μs, the density of H_2 is twice as high as the density of O_2. H_2 and O_2 density are also two orders of magnitude higher than the H_2O_2 density. The H_2, O_2 and H_2O_2 densities produced in this thermal plasma setting correspond to the densities predicted in the plasma kinetics simulation of the nanosecond pulsed discharge within 13% difference (See Figure 4.7). In conclusion, the production of H_2, O_2 and H_2O_2 is not very sensitive to the exact radical density during the discharge pulse. At high specific energy, H and O radical densities are very high during the discharge pulse and will recombine to H_2 and O_2. The high atomic densities and gas temperatures also disfavor

the formation of H_2O_2 leading to significantly less H_2O_2 production compared to H_2 and O_2.

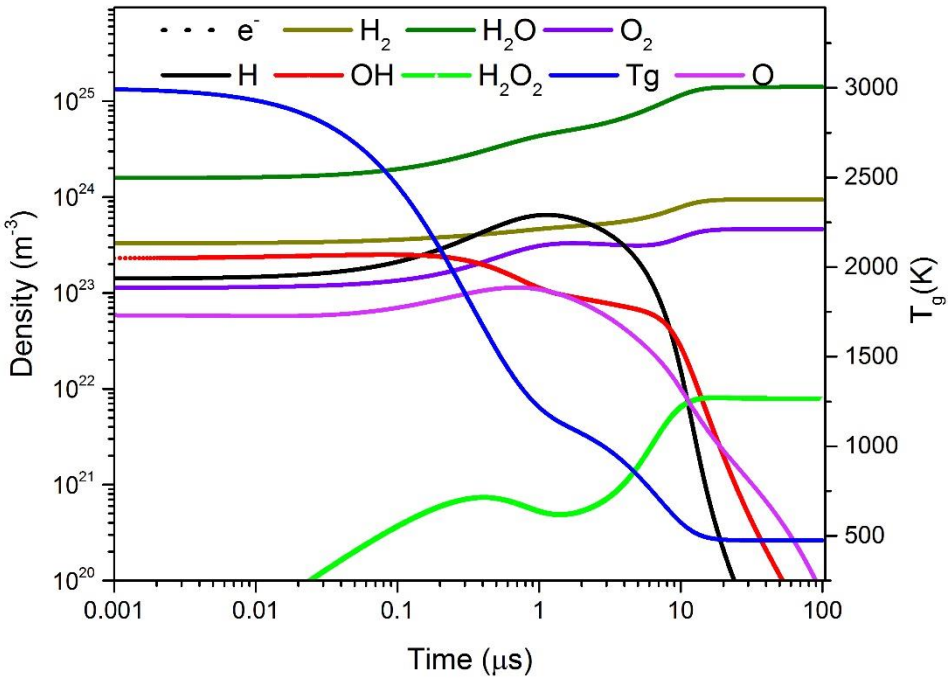

Figure 4.9 Main species at the constant pressure process when using the thermal equilibrium composition of water vapor at 3000 K as the input gas composition

4.6 Conclusion

In this chapter, the reaction set developed for the high electron density (~10^{22} m^{-3}) Ar + 0.1% H_2O discharge has been updated to enable its use for pure water vapor discharges at high specific energy. H and O are the two dominant radicals in the afterglow of the nanosecond pulsed high electron density pure water vapor discharge similar to the high electron density discharge in Ar with small amount of water vapor (< 1%). However, due to the increased water fraction in the gas mixture, the H and O densities are higher than the electron density during the discharge and reactions of H and O with H_2O become the dominate OH production mechanisms together with the direct electron dissociation of H_2O. The specific energy per water molecule at which the OH

density becomes lower than the O density is remarkably similar in the high electron density nanosecond pulsed pure water discharges (0.75 eV/molecule) and the high electron density nanosecond pulsed Ar + 0.1% H_2O discharge (0.83 eV/molecule). The fast heating mechanism due to the three-body recombination between H and OH radicals in the presence of water and the hydration reaction of O_2^+ ion increases the gas temperature by 1000 K within 10 ns and leads subsequently to significant thermal induced reactions in the plasma. The long-lived species (H_2, O_2 and H_2O_2) produced at high specific energies nanosecond pulsed discharges in water vapor is very similar to species produced by the recombination of thermal equilibrium composition of water vapor at the same thermal boundary conditions. This suggests that for high specific energy nanosecond pulsed discharge the production of long-lived species is insensitive to the exact radical composition during the pulse due to the non-selective nature of radical-radical reactions.

5 Nanosecond Pulsed Discharge in a Synchronized Helium Bubble: Memory Effects and Plasma Morphology

5.1 Introduction

Electrical discharges in bubbles have been studied due to their ability to produce reactive species to be used in applications ranging from water treatment and material processing to chemical synthesis and conversion [6,36,37]. While direct discharges in water have been extensively studied in the context of water treatment, energy efficiency is insufficient for large scale applications [5]. To improve the energy efficiency, discharges in water-containing bubbles have been proposed [38,39,40,41]. The ignition of discharges in the gas phase reduces energy losses by evaporation not used for reactive species production and has a lower breakdown voltage [29,42].

Nanosecond voltage pulses are often used to generate discharges in liquids and bubbles [12,43]. This not only reduces Joule heating in the conductive liquids but also, similarly to gas phase discharges, higher reduced electric fields lead to more energetic electrons favoring ionization and the production of reactive species rather than gas heating. Single nanosecond pulsed discharges in bubbles have been studied experimentally [44,45] and by simulations [15,16]. Previous work shows that the discharge in gas bubbles in water are typically filamentary surface discharges [44,46, 47]. Optical emission spectroscopy measurements have indicated a typical electron density range between 10^{20} and $10^{23} m^{-3}$ [10,48,49] and a gas temperature between 300 and 3000 K.

In gas phase discharges, the effect of the pulse repetition rate (PRR) on nanosecond pulsed discharges has been studied extensively [50,51,52]. These studies, show that the discharge becomes stronger with and increase in the PRR, which is usually referred to as a “memory effect” and can be due to pre-ionization left-over from the previous pulse, gas heating (increasing the reduced electric field for the same applied electric field) and the presence of negative ions and metastable species as sources of electrons through processes with a smaller energy threshold than electron impact ionization processes of ground state atoms or molecules [1]. Nonetheless, most detailed studies of discharges in bubbles are limited to single discharges most likely due to challenges to control and stabilize bubbles for multiple discharge events [44,53,54].

Similarly, glow-to-spark transitions have been extensively studied in gas phase glow discharges near or at atmospheric pressure [55,56,57,58,59,60]. The constriction of the discharge, preceding the spark formation, can be initiated at the anode, in the mid-gap and at the cathode. Replacing a metal electrode with a liquid water electrode has shown an increased stability of the glow discharge. The contraction of the glow discharge starts in this case near the metal electrode [61,62]. Most of the discharges in bubbles have been reported to be filamentary [44,46,47]. Changes in discharge morphology due to discharge mode transitions and instabilities have not been studied. Also models of discharges in bubbles have been predominantly modeled in 2D [46,53,63,64] while such transitions are intrinsically 3D phenomena.

In this paper, we report on the memory effect of repetitive pulsed discharges in a single helium bubble including the transition from a diffuse to filamentary discharge. A time-controlled helium bubble production was achieved at a

capillary nozzle by a solenoid valve and the discharge was time-synchronized with the bubble generation process. The nanosecond pulsed discharges in the bubble are investigated by ICCD imaging and current and voltage measurements allowing us to compare discharge morphology and power for different voltage pulse frequencies.

5.2 Experimental setup and methods

The setup used to generate nanosecond pulsed discharges in a bubble is shown in Figure 5.1. We synchronized the bubble generation with the discharge to enable discharge generation in a bubble of a fixed size and investigated memory effects impacting consecutive discharge pulses. The helium bubble was generated at the outlet of a quartz tube with an inner diameter of 1 mm and outer diameter of 3 mm at a frequency of 5 Hz in a NaCl solution with an electrical conductivity of 40 μS/cm. A stainless-steel wire with a diameter of 0.8 mm was inserted into the tube and used as an electrode. The wire tip was 1 mm below the nozzle and sharpened to locally enhance the electrical field and facilitate discharge formation. A ground electrode was inserted in the liquid vessel at a distance 5 cm from the bubble.

The supply of He through the quartz tube was controlled by a solenoid valve (USG2M51 24V, CKD). Voltage pulses were applied to the wire by a DEI PVX-4110 high-voltage pulse generator controlled by a function generator (Tektronix AFG 3051C). The high voltage to the DC pulser was supplied by a Spellman SL300 DC high voltage power supply. The pulses were synchronized with the bubble generation by a delay generator (BNC 577) in burst mode. The pulse voltage amplitude was fixed at 5 kV with a duration of 5 μs unless otherwise reported. The frequency of the voltage pulses in one burst was adjusted between 100 Hz and 10 kHz set with a function generator (Tektronix AFG

2021). A 1 kΩ high voltage resistor was connected between the high-voltage output of the pulse generator and the end of the wire in the capillary tube to ensure the current remained below 5 A.

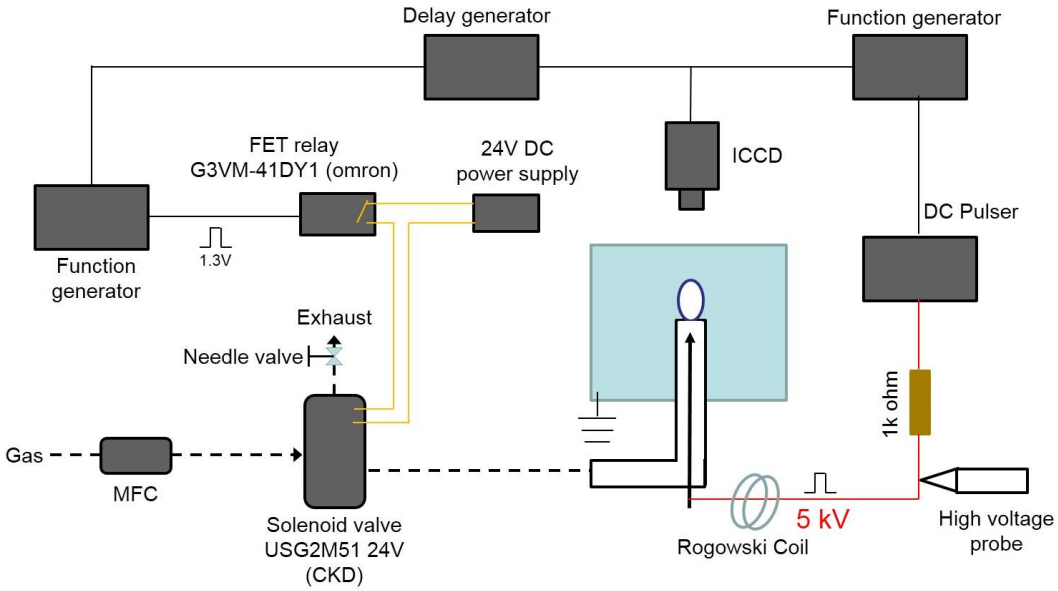

Figure 5.1 Schematic of Bubble Discharge Generation System

A high voltage probe (Tektronix P6015A) and Rogowsky coil (Pearson 2977) were used to measure the voltage and current waveforms. As shown in Fig. 5.2(a), the peak power within the first 150 ns time window was calculated by multiplying the measured voltage and current waveforms and was defined as the ignition power of the discharge in this chapter. The two maxima in the current peak are due to a capacitive current (first maximum) and a conduction current (second maximum). Images were taken single-shot with a gate of 150 ns using an ICCD camera (Andor iStar DH340T). The bubble shape and dynamics were monitored with a fast framing camera (Photron FastCam MINI).

5.3 Results and discussion

5.3.1 Memory effect

The results in Figure 5.2(b) show the effect of the bubble size on the discharge emission profile. The change in bubble size is achieved by varying the delay between the voltage pulse and the moment at which the previous bubble detaches from the capillary. We use the ignition power to quantitatively assess the effect of the bubble size and memory effect on the plasma generation. The ignition power of the bubble discharge increases with increasing bubble size and reaches a steady state value of 7.2 kW for $t \geq 73$ ms. For this reason, all experiment results in this study, were obtained at a fixed delay of 73 ms after the detachment of the previous bubble.

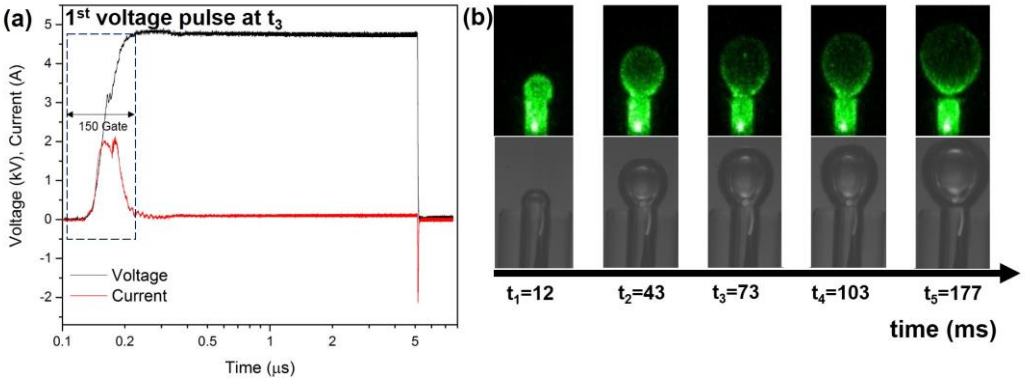

Figure 5.2 (a) Voltage and current waveforms of the first pulse for a positive polarity discharge in a helium bubble with a diameter of 2.5 mm. The ICCD gate is also indicated in dashed black box. (b) Images of the bubble and emission during the first current pulse of a positive polarity discharge in bubbles with different size recorded with a time delay the voltage pulse relative to the gas injection time as indicated. The time at which the previous bubble detaches from the capillary is set as t = 0 ms. The outer diameter of the capillary is 3 mm.

We applied a burst of 10 voltages pulses in one bubble and the time between pulses was varied in the range of 0.1 to 10 ms corresponding to a repetition rate from 10 kHz to 100 Hz. Figure 5.3 compares the ignition power of the first and second voltage pulse in a single bubble as a function of the pulse period for both positive and negative voltage polarities. The ignition power of the first pulse is always significantly higher than for the second pulse when the period is less than 1.25 ms or 1 ms for positive and negative polarity, respectively. This observation is opposite to the typical increase in energy found for nanosecond pulsed discharges at high repetition rates in e.g. pin-pin geometries [50,52]. The cause of the memory effect leading to a reduction in ignition power has a lifetime of approximately 1 ms and hence could be due to a change in gas composition (such as an increase in water vapor which will enhance electron loss by attachment) and surface charging on the bubble wall or capillary tube which could effectively reduce the applied electric field. In the following, both possibilities are analyzed in detail to determine the cause of the observed effect.

The charge relaxation time of surface charge at the bubble interface can be estimated by the charge relaxation time of the NaCl solution [65]

$$\tau = \frac{\varepsilon}{\sigma} = 170 \text{ ns} \qquad (5.1)$$

Since the charge on the bubble wall can be removed on a sub-μs time scale, the effect of charge on the bubble wall will not contribute to the observed memory effect on a time scale of 1 ms.

Next, we assess the effect of an increase in water vapor. We first assess the

initial water concentration in the gas bubble. The time it takes a helium bubble submerged in water to become saturated with water vapor at room temperature can be estimated by the diffusion time constant of a sphere [66]

$$t = \frac{0.5\,R^2}{D_{H_2O-He}} = 37\ \text{ms} \qquad (5.2)$$

The diffusion coefficient of H_2O in the He ($D_{H2O\text{-}He}$) is taken from [67] and bubble radius (R) is 2.5 mm. As this is a factor of 2 smaller than the time difference between the start of the bubble generation and the voltage pulse i.e.73 ms, the bubble is saturated with water vapor before the ignition of the first discharge in the burst.

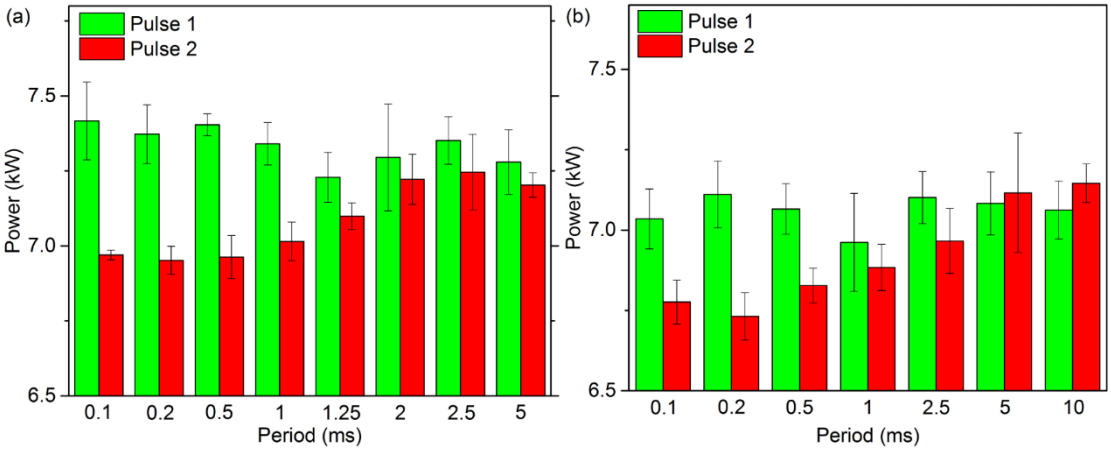

Figure 5.3 Ignition power comparison between the first and second voltage pulse in a single bubble as a function of the pulse period for positive (a) and negative (b) voltage pulses.

The gas composition can however be influenced by the gas temperature as well. The gas temperature measured by optical emission of similar pulsed helium discharge is 450 K [48]. This is however the gas temperature in a plasma filament and the averaged gas temperature in the bubble is expected to be much lower. While an increase in gas temperature by the plasma pulse,

for a given gas composition, would lead to an increase in intensity of the subsequent discharge (due to higher reduced electric field at a fixed electric field), it would also enable a water vapor pressure inside the bubble in excess of the room temperature vapor saturation pressure. If the entire energy of a single discharge pulse is used to evaporate water, the water vapor concentration can increase by a factor of 2 which is possible in a bubble with a temperature of 315K.

To enable us to assess the dominant effect of changes in water vapor concentration a reference experiment was conducted by using the same experimental setup however with the following changes: the amount of liquid solution in the reactor is reduced so only reaches up to 1 mm below the nozzle of the quartz tube, a dry helium gas feed of 1.5 slm through the capillary was applied and a tungsten rod as grounded electrode covered with a 500 μm thickness alumina plate was placed 2.5 mm above the capillary tube. Figure 5.4 shows the recorded current-voltage waveform for this reference setup. The difference in the ignition power between the first and the second pulse remains although for a pulse period smaller than 0.5 ms. This allows to conclude that changes in water vapor concentration are not required to cause the observed memory effect. Nonetheless the breakdown seems delayed compared to the discharge in a bubble (the conduction current peak is delayed with 250 ns compared to the rise time).

Based on the above analysis, the surface charge on the quartz tube wall seems the main contributing factor in the observed memory effect. The effect of surface charge on the micro-discharge formation in DBD's can last for several microseconds up to even milliseconds in the afterglow [11,68,69,70]. Unfortunately, it is hard to predict the surface charge distribution on the quartz

tube wall due to the recombination and diffusion of ions in the tube from the previous discharge [71], as it depends on many parameters including surface properties and gas impurities which makes a quantitative analysis unfeasible. Nonetheless the dominant mechanism responsible for the observed effect that occurs for both positive and negative polarity discharges, is consistent with a similar observation or similar time scales in a DBD [68]. The surface charge produced by the previous discharge accumulated on the surface of the quartz wall reduces the local electrical field around the needle electrode and reduces the intensity of the subsequent. This mechanism can also explain the observed memory effect in the bubble experiment and the dry helium jet in the reference experiment. The smaller time scale at which the memory effect is no longer observed for the dry helium case compared to the bubble case might be due to the reduced mobility of ions due to hydration of ions in the presence of water vapor [72].

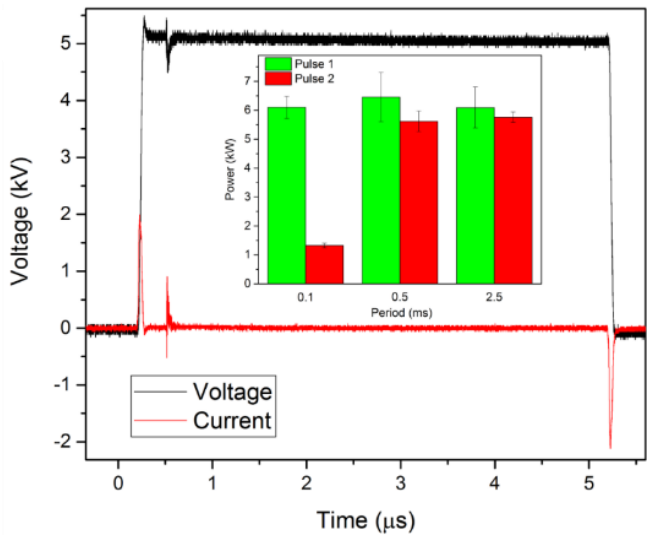

Figure 5.4 Voltage-current waveform of the positive polarity discharge in the capillary jet configuration. The insert shows the ignition power of the first and second voltage pulse for different pulse periods.

5.3.2 Transition from diffuse to filamentary discharge and polarity dependences on discharge morphology.

Figure 5.5 shows images of the bubble discharge at the rising and falling edge of the voltage pulse for both positive and negative polarities in the first, second, fifth, seventh and tenth pulse in a single bubble. The pulse duration is 5 μs and the burst of 10 pulses is generated at a frequency of 10 kHz. The discharge is diffuse during the rising edge of the voltage pulse for both polarities, while during the falling edge of the voltage pulse, the discharge is filamentary. Filamentary discharges are only observed when the pulse width is larger than 2 μs for both positive and negative polarities (not shown). This is consistent with the time scale of a transition from glow to a spark discharge in a pulsed discharge in helium generated between a metal pin electrode and a water surface [62]. This transition most likely occurs because of an ionization instability due to stepwise ionization and/or gas heating processes [1]. The transition from a diffuse to filamentary mode is most clear in the first pulse but is less pronounced in the subsequent pulses. This is caused by pre-ionization due to of the previous discharge pulses and/or a reduction in the electric field at ignition due to surface charging as described above leading to a more homogeneous discharge [73].

Figure 5.5 also shows a significant difference in the plasma volume between the first and tenth pulse. The first pulse occupies a larger volume of the bubble than the tenth pulse for both positive and negative polarities. This is most likely caused by a local increase in water vapor near the liquid interface in the subsequent discharge pulses reducing the effective ionization rate at moderate reduced electric fields due to an increase in attachment rate with increasing H_2O.

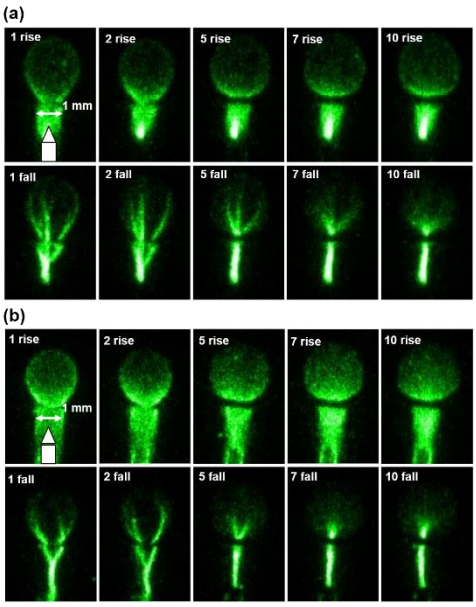

Figure 5.5 (a) Time evolution of the positive polarity and negative polarity (b) of the bubble discharge. The images labeled “rise” were recorded at the rising edge of the voltage and the images labeled “fall” were taken at the falling edge of the voltage with an ICCD gate of 150 ns for the 1st, 2nd, 5th, 7th and 10th pulse. The burst of 10 pulses applied is generated at a frequency of 10 kHz. The length scale of 1 mm represents the inner diameter of the quartz tube and the location of the needle is shown in the first image.

A distinctive difference between the negative and positive polarity discharge is that the negative polarity discharge has a stronger emission between the needle and capillary tube while the positive discharge is mainly located between the needle tip and the bubble. The emission of the negative discharge is also more homogeneous than the positive discharge. This is consistent with the observed difference in the breakdown voltage in asymmetric DBD for positive and negative polarities in concentric metal wire electrode dielectric tube geometry [74,75]. Indeed, when the wire acts as cathode, secondary electron emission from the metal cathode enables a supply of secondary

electrons and hence more seed electrons are available to sustain a discharge compared to when the cathode is the dielectric.

5.4 Conclusion

In this work, we reported on the memory effect and discharge morphology respectively in micro-second pulsed discharges in a single helium bubble generated at the tip of a capillary containing a high voltage needle. The primary reason for the observed memory effect in bubbles reducing the ignition power of the discharge is related to surface charging on the quartz tube capillary used to supply the helium gas. This effect is similar to the effect found in DBDs and lasts up to 1 ms. The transition from a diffusive to filamentary discharge was observed on the time scale of 2 μs consistent with a previously observed glow-to-spark transition in the gas phase. In addition, a reduction of the filamentary nature of the discharge was observed due to the pre-ionization and/or a reduction of the electric field due to surface charge accumulation at high pulse repetition rate. This study shows that, for the observed phenomena, discharges in helium bubbles behave very similar to bulk gas phase discharges.

6 Characterization of Discharge in Liquid and Power Measurement

6.1 Introduction

Discharges in liquid are typically streamer-like discharges generated by pulsed high voltages at a sharp high voltage pin electrode. Decades of research and study lead to a global understanding of such discharges. Pulsed discharges in liquid have electron density in the range of 10^{24} - 10^{26} m^{-3}[10]. The pressure during discharge ignition can be as high as 1 GPa and the gas temperature has been reported to be in the range of 1000 – 7000 K [10]. The discharge deposits energy between 1 mJ and 1 J per pulse. Discharge channels can have a diameter of 20 µm, resulting in a power density up to tens of GW/m^3 [10]. The initialization of the plasma is highly dependent on the characteristics of the high voltage pulse. To date, no comprehensive theory of the plasma formation in liquid is available. In general, plasmas in liquids have not been well characterized due to many challenges for diagnostics [10]. The main challenges of characterizing liquid discharge are due to the jitter of plasma formation in time and the random filament formation in space. These streamers are usually branching randomly and hard to study experimentally [8]. Due to the complex and random nature of the discharges in liquid, it is very important to create a temporally (remove jitter) and spatially (remove random filaments) stable discharge for the sake of diagnostics. In this chapter, we show the design of an experiment system producing temporally and spatially stable discharges in water and introduce electrical diagnostics to measure the power deposition into the plasma formed in the liquid phase.

6.1.1 Plasma source

A single pin electrode geometry was used in the experiment to create plasma in a NaCl solution with an electrical conductivity of 200 μS/cm. The produced corona-like discharge was initialized at and located near the pin electrode and the metal chamber was grounded.

The schematic of the discharge chamber and coupling to the power supply is shown in Figure 6.1. The HV pulser (FPG 50-1NM12) was used to produce a positive voltage pulse with maximum amplitude of 50kV, rise time of 3-5 ns and pulse duration (FWHM) of 12-15 ns. The high voltage pulse was delivered to the home-made coaxial rod vessel assembly (RVA) by a 50 Ω transmission line (coaxial cable). A high voltage insulated connection was used to connect the transmission line to the RVA. A sharp tungsten needle was tightly fitted into a tap hole on the top of the rod and served as the high voltage electrode (anode) to generate the plasma in the liquid. The RVA delivered the high voltage pulse to the anode for plasma generation in the plasma reactor and was equipped with home-made voltage and current sensors. There were three quartz windows mounted on the plasma reactor which provide optical access for diagnostics. The layout of the reactor and orientation of the window can be seen in Figure 6.2.

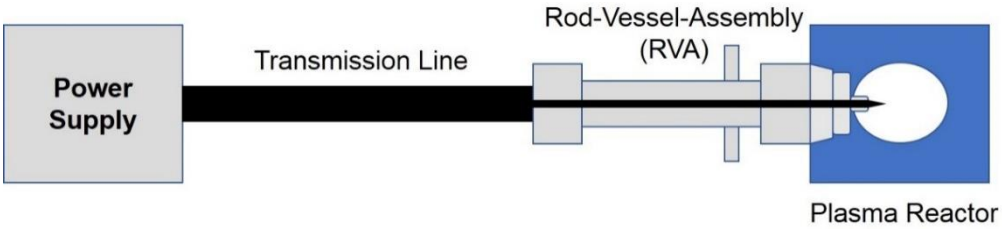

Figure 6.1 Schematic of the discharge-in-liquid setup

To achieve the formation of a discharge without jitter, nanosecond voltage pulses were employed. Since the microsecond or millisecond pulses vaporize the water and create microbubbles, the discharge generation is prone to be influenced by the fluctuations in phase change and the presence of bubbles, which are randomly distributed in the water and uncontrollable. On the other hand, nanosecond voltage pulses provide a strong localized electrical field at the pin electrode that can generate a plasma directly in the liquid without significantly heating a large volume of water [76]. The nanosecond high voltage pulse can be externally trigged, and time synchronized with an ICCD camera to perform optical diagnostics using a BNC 577 delay generator.

The use of a single pin in this experiment to produce corona discharge in liquid water enables the generation of a spherical corona-like discharge at a fixed position at the anode.

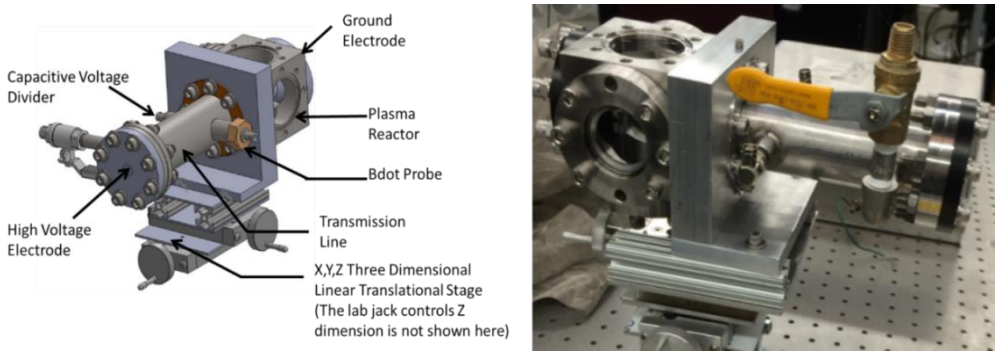

Figure 6.2 The 3D drawing of the setup (left) and photo of the setup (right)

6.2 Transmission line theory

The coaxial cable used with an inner core and cylindrical surrounding is a transmission line. The dielectric material between the two metals creates distributed capacitors between them and the metal itself introduces an

inductance if the size of the metal is not negligible. The equivalent circuit of the transmission line can be seen in Figure 6.3. It is assumed that the transmission line is lossless, namely no resistance is present in the transmission line. From the power source (left side of the figure) to the load (right side of the figure), the power is delivered block by block (the block is shown as a green dashed square) by charging and discharging the capacitors in the block. When the energy transfers to a block, a back-current (black arrow) emerges on the portion of the ground line belongs to that block of the transmission line. Due to the charging process of the capacitor, such current has the same amplitude as the current in the high voltage central rod (labeled in red) but has an opposite direction, and that is where the name back-current comes from. This phenomenon can be used in measuring the current flowing through the center rod, which is usually in the order of kA for discharges generated in liquid.

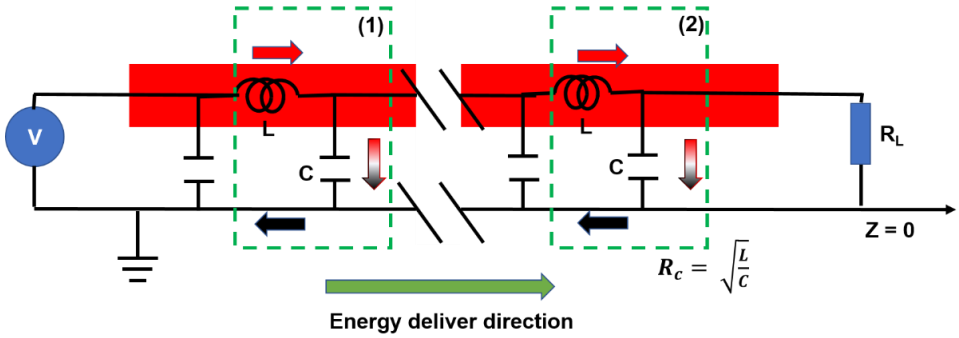

Figure 6.3. Schematic of the energy transfer in transmission line

The energy is delivered in the transmission line in the form of an electromagnetic wave. There are two waves travelling in the transmission line: the forward and reflected wave. The forward wave originates from the power source and the reflected wave is reflected from the load. At any position in the transmission line, the voltage and current are the superposition of these two opposite-directional waves. The superscript '+' represents the forward wave

and the superscript '–' represents the reflected wave. u is the propagation speed of the travelling wave and Z is the impedance of the transmission line. L and C are the inductance and capacitance per unit length of the transmission line. The origin of the z-axis (z = 0) is set at the position of the load.

$$V(z,t) = V^{+}(t - z/u) + V^{-}(t + z/u) \quad (6.1)$$

$$I(z,t) = I^{+}(t - z/u) - I^{-}(t + z/u) \quad (6.2)$$

$$u = \frac{1}{\sqrt{LC}} \quad (6.3)$$

$$Z = \sqrt{\frac{L}{C}} \quad (6.4)$$

The characteristic (amplitude and polarity) of the reflected wave is strongly related to the load. If the impedance of the load is the same as the impedance of the transmission line, the load is called matched. In this scenario, the reflection is zero, there is no reflected wave. If the load is infinitely large which is used to simulate an open-end cable, the reflection is the strongest. The entire forward wave is reflected. The voltage of the reflected wave has the same amplitude and the same polarity, and the current has the same amplitude but opposite polarity. If the load impedance is zero, which represents a short-circuited cable, the reflected wave has a voltage with the same amplitude and opposite polarity and a current with the same amplitude and the same polarity. In short, the open-ended transmission line doubles the voltage at the load end and a short-circuited transmission line doubles the current. The parameter Γ, the reflection coefficient is defined in (6.5). Z_L is the impedance of the load and Z_C is the impedance of the transmission line.

$$\Gamma = \frac{V^{-}(t+ z/u)}{V^{+}(t- z/u)} = \frac{-I^{-}(t+ z/u)}{I^{+}(t- z/u)} = \frac{Z_L - Z_c}{Z_L + Z_c} \quad (6.5)$$

When the load end is terminated with an impedance matched load ($Z_L = Z_C$), the reflection coefficient is zero; when the load end of the transmission line is open ($Z_C >> Z_L$), the reflection coefficient is 1; when the load end of the transmission line is a short-circuit ($Z_L = 0$), the reflection coefficient is -1. V_0 and I_0 are the voltage and current waveform at z = 0 position, namely at the load of the transmission line, which are shown in (6.6) and (6.7).

$$V_0(t) = (1 + \Gamma)V^+(t) \quad (6.6)$$

$$I_0(t) = (1 - \Gamma)I^+(t) \quad (6.7)$$

6.3 Power measurement system for the discharge in liquid

The accurate power measurement is crucial to control the experimental conditions quantitatively. However, the nanosecond pulsed discharge generated in water yields new challenges for the power measurement. In order to record the nanosecond power deposition to the liquid discharge, the sensor needs to have a high bandwidth of GHz and be built-in into the setup. To capture the GHz frequency content of the pulse, the sampling frequency needs to be at least a factor 2 higher than the frequency of the pulse according to Nyquist Theorem. Besides, the built-in feature enables the development of a well-shielded setup to limit the influence of the electromagnetic interference (EMI) to the minimum level. The commercially available voltage and current sensors, either do not have high enough bandwidth to resolve the nanosecond scale signal or introduce practical issues such as EMI shielding.

To meet the requirements of the power measurement system described above, a home-made power measurement system was established by adapting a customized back-current shunt (BCS) and designing and manufacturing a rod-vessel-assembly (RVA) system that enabled the introduction of a home-made

Ddot and Bdot to mount on. The RVA was filled with transformer oil (μ_r = 1, ε_r = 2.2) and the impedance of the RVA was designed to be 50 Ω, which is the same as the coaxial cable provided by FID. It is essential to keep the impedance of the RVA the same as the impedance of the FID transmission line to increase the energy transfer efficiency and reduce the unnecessary reflection at the FID coaxial cable/RVA connection. In this section, the design of the RVA is introduced first and followed by the BCS, Ddot and Bdot working principles.

6.3.1 Design of the RVA

The impedance of a coaxial transmission line can be calculated using equation 6.8. μ_r is the relative permeability, ε_r is the relative permittivity of the dielectric material of the transmission line and r_o and r_i are the radius of the ground electrode and power electrode in a coaxial layout, respectively.

$$Z = 60(\mu_r/\varepsilon_r)^{\frac{1}{2}} \ln(r_o/r_i) \qquad (6.8)$$

The RVA was designed in a coaxial cylindrical shape. An aluminum solid rod (O.D. = 0.5 inch) was placed at the center of a hollow stainless-steel cylindrical vessel (I.D. = 3.38 inch). The vessel was filled with transformer oil, which acts as the dielectric material between the center rod and the vessel. The RVA is thus a transmission line. Two short stainless-steel tubes were welded on the vessel close to the needle position (~10 cm). The Ddot and Bdot were mounted in the stainless-steel tube using thread connection and O-rings were used to prevent oil from leaking out of the vessel through these connections. The RVA was connected to the plasma reactor by screws. The RVA was designed as an easy-to-mount and easy-to-shield transmission line for Ddot and Bdot sensors.

6.3.2 Voltage and current measurement theory

Power measurements were conducted through measuring voltage and current of the discharge directly or indirectly using BCS, Ddot and Bdot.

The BCS measures the forward and reflected current waveform in the high voltage central rod. Since the impedance of the transmission line (50 Ω) is known, by multiplying the current signal obtained from the BCS with the impedance, the voltage waveform in the high voltage central rod can be retrieved as well. The only challenge of using the BCS for power measurements is to separate the forward and reflected pulse train. As we know from the transmission line theory, at any position in the transmission line, the voltage and current waveforms are the superposition of the forward and reflected components. The details of separating forward and reflected waves is introduced in the later sections. Once the forward (I^+) and reflected (I^-) current waveform are separated from the BCS signal, power can be calculated using Eq.9, where I^+ and I^- are the forward and reflected current in the high voltage central rod, Z_c is the impedance of the transmission line. The power difference between the forward power and the reflected power is the upper limit of the power deposition in the plasma. There might be other losses of the power, such as heat transfer and ohmic heating in the transmission line. $\tilde{z}$ is the distance from the BCS to the tip of the anode needle.

$$P = I^+(t - \tilde{z}/u)^2 R_c - I^-(t + \tilde{z}/u)^2 R_c \qquad (6.9)$$

Once the Ddot and Bdot are calibrated, the voltage and current in the high voltage central rod close to the anode needle can be measured using these two sensors. Assuming the cable is open-ended when the corona plasma is generated, the polarity of the forward and reflected voltage are the same and

the forward and reflected current have opposite polarity.

$$P = \left(U^{+}(t - z_0/u) + U^{-}(t + z_0/u)\right) * \left(I^{+}(t - z_0/u) + I^{-}(t + z_0/u)\right) \qquad (6.10)$$

Eq. 6.9 and Eq. 6.10 could lead to different result and will be estimated in the experimental case study.

All three sensors were employed in the experiment. In general, as a good practice to achieve a short response time, the sensors were designed to have a low inductance to prevent significant time lag caused by the inductance effect. In general, each sensor used in the experiment has limitations. The BCS measures the forward current waveform and reflected current waveform. When the transmission line is not long enough, the forward and reflected waves overlap with each other and are difficult to separate. The mounting of the BCS also requires to destructively open and modify the transmission line, which induces risks of introducing weak points in the cable that can lead to breakdown. A challenge for the BCS is the measurement of the long-lasting reflection in voltage and current waveforms, which usually exists in discharge in liquid when the load (impedance of water) is highly nonlinear. The nonlinearity comes from the fact that the discharge can highly impact the impedance of the load. However, for a localized plasma as in this study the effect is less than for a spark generated between two pin electrodes. In the experiment, we observed the reflection of the voltage/current wave can last for almost 4 μs. Given the value of the electromagnetic wave travelling speed in the transmission line is in the order of 2×10^8 m/s, to separate the whole forward and the reflected wave (the wave duration is ~ 4 μs) the cable length needs to be at least 400 m, which is unpractical. In order to separate the

forward and reflected wave in the transmission line and keep the transmission line at a reasonable length, the Ddot was used along with the BCS. Using Ddot and Bdot together is another way to measure the long-lasting reflection voltage/current waveforms without any requirement for the length of the transmission line. The calibration process for Ddot and Bdot is not trivial. The coefficients of Ddot and Bdot are both geometry and frequency dependent. Since the dimension of the sensors are hard to be measured accurately (handmade) and the pulse rise time is amplitude dependent (different voltage amplitudes have different rise time), the coefficients are difficult to obtain analytically and need to be determined under the frequency used in the experiment condition.

6.3.3 Back-current Shunt (BCS)

The BCS is a mature technique [77,78]. It is usually embedded in the transmission line by soldering in the shielding layer. As shown in Figure 6.4, a typical transmission line consists of three to four layers, the inner layer is the metal rod, the intermediate layer is a layer of dielectric material (varying from manufacturer to manufacturer) and the outer layer is the mesh shielding layer. Sometimes a rubber coat is added to the outmost layer as a protection of the mesh. It is optional and only acts as a protection of the mesh shielding.

In the process of making a BCS, a segment of the shielding layer of the transmission line needs to be peeled off and several low inductance resistors are welded in parallel to connect the two ends of the shielding mesh. The resistors are arranged in the circumferential direction sitting at the outer surface of the dielectric layer of the transmission line. The schematic of the BCS used in this experiment is shown in Figure 6.4.

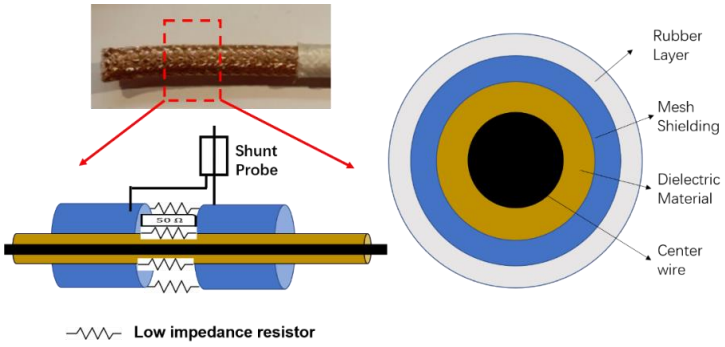

Figure 6.4 Schematic of the BCS structure and layout in transmission line

Based on the transmission line theory, the back-current has the same amplitude as the current flowing in the high voltage central rod. The back-current can be retrieved by measuring the voltage across the known resistor (the resistors welded in the shielding mesh) through which current passes. The equivalent circuit of a BCS is shown in Figure 6.5 (assuming a lossless transmission line) and the relation between the measured voltage (V_{shunt}) and the high voltage electrode current (I_{core}) is established in equation 6.11, 6.12 and 6.13. By using Eq. 6.13, the current flowing in the center electrode can be derived from the BCS readout as long as the resistor of the shunt is known. In the experiment, the BCS was manufactured and provided by FID without the value of the resistance of the shunt was unknown to us and required calibration.

$$I_{core} = -I_{back} \tag{6.11}$$

$$I_{back} = \frac{V_{shunt}}{R_{shunt}} \tag{6.12}$$

$$I_{core} = -\frac{V_{shunt}}{R_{shunt}} \tag{6.13}$$

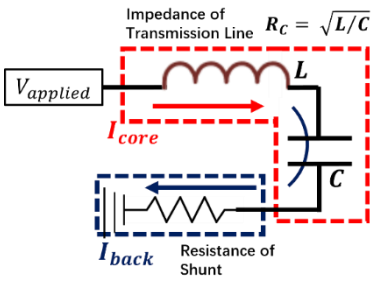

Figure 6.5 The equivalent circuit of a BCS

The Ddot and Bdot working principals have been reported in [79]. In the current work, the principles of the Ddot and Bdot are identical but the structures of the sensors are different.

6.3.3.1 Ddot

A strong electrical field is essential to generate plasmas in liquid water. It requires applying tens of kV's voltage pulses to a sharp needle. However, the oscilloscope is only able to measure voltage waveforms with maximum voltage amplitude of 50V.

A voltage divider enables to reduce the amplitude of a high voltage signal to a value consistent with the input requirements of an oscilloscope. The Ddot is a specific kind of voltage divider we employed in this experiment. The schematic of a Ddot is shown in Figure 6.6. C_H is the capacity between the central wire tip of the Ddot and the high voltage central rod, C_E is the capacity between the Ddot central wire and ground. These two capacitors are connected in series. C_E is designed to be much larger than C_H. As a result, the voltage across capacitor C_E is much smaller than the high voltage and can be safely measured by the oscilloscope. Z is the impedance of the diagnostic system. The relation between the measured Ddot voltage (u) and applied voltage (V) is described in Eq.6.14, 6.15 and 6.16. To simplify the equation, B is defined as the sum of

C_E and C_H. When $\omega B \gg 1$, the measured voltage of the Ddot and the applied high voltage have a linear relation, and we call this frequency “linear region”. On the other hand, if $\omega B \ll 1$, the measured waveform is proportional to the integral of the applied high voltage, and we call this frequency “Integration region”. For frequencies in between these two limits, the applied high voltage can be reconstructed from the Ddot readout as a linear combination of the raw and the integrated Ddot signal shown in Eq. 6.16.

$$\mathrm{u(t)} = \frac{C_H}{C_H + C_E} U(t) \tag{6.14}$$

$$u = \frac{j\omega C_H Z}{1 + j\omega (C_E + C_H) Z} V = \frac{j\omega A}{1 + j\omega B} V \tag{6.15}$$

$$V = \left(\frac{1}{j\omega A} + \frac{B}{A}\right) u = A_{Ddot} \left(B_{Ddot} u + C_{Ddot} \int_{-\infty}^{t} u \, dt\right) \tag{6.16}$$

The coefficients of the raw signal and integrated signal of Ddot are frequency dependent and require a calibration in the same frequency roughly as for the planned experiment.

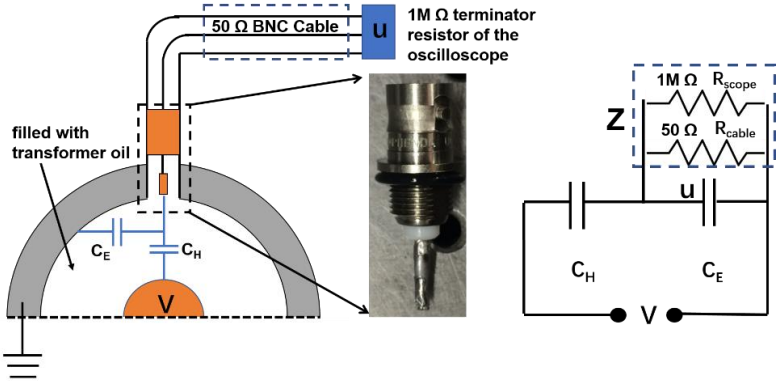

Figure 6.6 Schematic and equivalent circuit of Ddot

6.3.3.2 Bdot

The current flowing in the high voltage central rod can be measured by a BCS, but the use of the BCS has limitations when current pulses overlap. We use

the Bdot to measure the discharge current when the cable is short, or the reflection lasts long. The schematic of Bdot is shown in Figure 6.7. A Bdot is basically a metal (copper) wire loop. The Bdot wire loop was placed perpendicular to the direction of the magnetic field generated by the current in the core conductor to achieve sensitive current measurements. Once the magnetic flux through the loop changes, a current is generated in the loop to resist the change in magnetic flux through the loop. Hence there is a relationship between the measured voltage across the Bdot and the current flowing in the high voltage central rod.

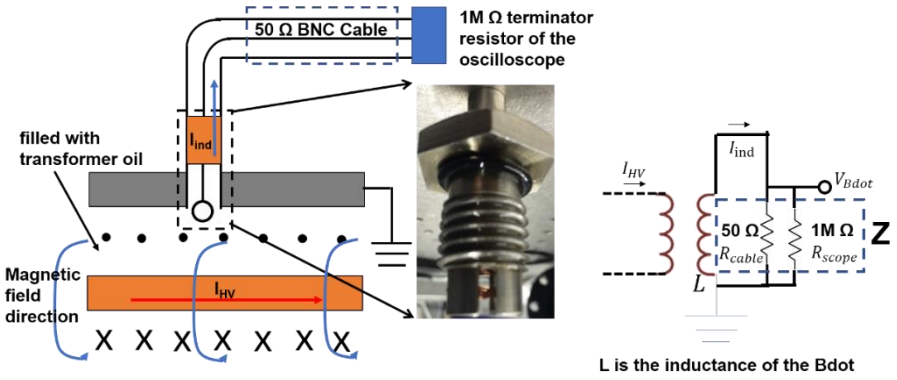

Figure 6.7 Schematic and equivalent circuit of Ddot

The equivalent circuit of the Bdot diagnostic system is also shown in Figure 6.7. The relation between the measured Bdot readout and the applied voltage is given in Eqs 17, 18 and 19. M is the coefficient mapping the primary current, the current flowing in the high voltage central rod to the secondary induced voltage and is called mutual inductance. It is determined by the geometry and structure of the Bdot. This includes the distance between the Bdot to the high voltage central rod, the number of loops of the copper wire, the properties of the transformer oil, etc. Like the Ddot system, when $\omega \frac{L}{Z} \gg 1$, there is a linear correlation between the

measured Bdot voltage and the current flowing in the high voltage central rod; when $\omega\frac{L}{Z} \ll 1$, the current in the high voltage central rod is proportional to the integral of the Bdot readout. A more general form that allows to deduce the current flowing in the high voltage central rod fro the Bdot signal (V_{Bdot}) can be found in Eq. 19. I_{HV} is a combination of V_{Bdot} and the integral of the V_{Bdot}. A_{Bdot}, B_{Bdot} and C_{Bdot} are three coefficients that are geometry and frequency dependent and need to be determined via a calibration process.

$$M\frac{dI_{HV}}{dt} = V_{Bdot} + L\frac{dI_{ind}}{dt} \tag{6.17}$$

$$V_{Bdot} = \frac{j\omega M}{1+j\omega\frac{L}{Z}} I_{HV} = \frac{j\omega C}{1+j\omega D} I_{HV} \tag{6.18}$$

$$I_{HV} = \left(\frac{1}{j\omega C} + \frac{D}{C}\right) V_{Bdot}$$

$$= A_{Bdot}\left(B_{Bdot}V_{Bdot} + C_{Bdot}\int_{-\infty}^{t} V_{Bdot}\,dt\right) \tag{6.19}$$

6.3.4 Calibration of the electrical measurement system

To obtain an absolute voltage and current measurement, calibration is needed to obtain the coefficients of the Ddot and Bdot and the value of the resistance of the BCS used in the experiment. The coefficient of the BCS is determined by the resistors welded in the shielding while the coefficient of the Ddot and Bdot are determined by the geometry of the homemade transmission line system and the working frequency of the experiment.

6.3.4.1 Calibration of the BCS

Since the BCS is made of resistors which are in good approximation frequency

independent. We can use a DC voltage supply to measure the resistance of the shunt. The anode of the DC voltage supply is connected to the central wire of the transmission line and the cathode to the ground of the transmission line. At the load, the central wire and the ground of the transmission line were connected with a 27.6 Ω resistor. The voltage at the BCS output was measured by a multimeter yielding a value of 42.6 mV and the voltage across the 27.6 Ω resistor was 2.94 V. In this case, the current flowing through the known value resistor was the same as the current flowing through the BCS, the resistance of the shunt was calculated as 0.4 ± 0.04 Ω.

6.3.4.2 Calibration of the Ddot

The calibration system of the Ddot is shown in Figure 6.8. We used the system identical to the setup for generating plasma as described above. The plasma reactor was filled with tap water (electrical conductivity ~200 μS/cm) to mimic the real experimental condition. A high voltage of 40 kV was applied (to calibrate the Ddot under the same experiment condition as the plasma generation condition) and a series of readouts from the BCS and Ddot were recorded. The voltage at the Ddot position can be reconstructed from the BCS signal. The calibrated shunt was used to calibrate the voltage waveform obtained from Ddot. A LeCory high resolution oscilloscope (wavesurfer10, 1 GHz) was employed to record both BCS and Ddot's readouts.

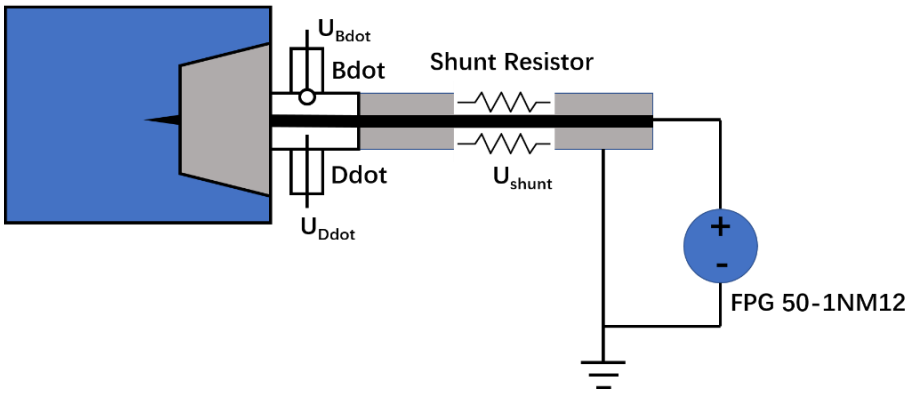

Figure 6.8 Calibration System of the Ddot and Bdot

Only the first two peaks of the forward voltage waveform captured by the BCS were used in the calibration since the subsequent voltage peaks had overlapping forward and reflected voltage peaks. The detailed calibration procedure and the schematic is shown in Figure 6.9. All the waveforms in Figure 6.9 are normalized. As shown in Eq.6.16, there are three coefficients need to be determined. B_{Ddot} and C_{Ddot} determine the waveform shape of reconstructed voltage signal from the Ddot measurement, which can be derived by comparing the normalized Ddot raw signal waveform and the normalized Ddot signal integral waveform in Figure 6.9. It turns out that the contribution of the Ddot raw signal to the reconstructed voltage is negligible for the experimental condition used (3~5 ns rise time, 40 kV). By setting B_{Ddot} to zero and C_{Ddot} to one, a good fit between the reconstructed Ddot voltage waveform and the BCS voltage waveform was observed for the first and second peak of the forward voltage waveform. It is safe to conclude that the Ddot sensor can predict the shape of the waveform by integrating the raw signal measured in the experiment when the applied voltage is 40 kV. The coefficient A_{Ddot} was obtained by comparing the Ddot signal integral with the amplitude of the measured voltage through BCS. Assuming the spherical plasma at the anode is equivalent to an open load, the Ddot measures the supposition of the forward and the reflected voltage waveforms in an open-

ended coaxial cable which can be extracted from the BSC waveform.

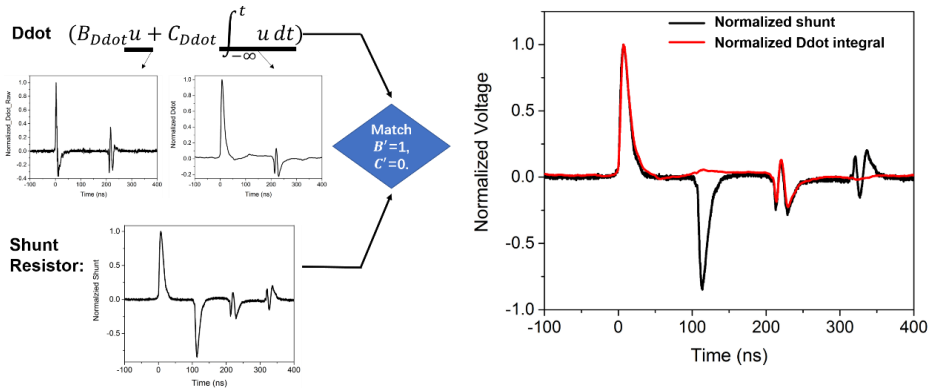

Figure 6.9 Schematic of the Ddot calibration procedure

The method to separate the forward and reflected waveform in the BCS will be introduced in the later sections. As a result, the coefficient A_{Ddot} of the Ddot is $(1.30 \pm 0.13) \times 10^{12}$ V/V for the experiment condition (3~5 ns, 40 kV).

6.3.4.3 Calibration of the Bdot

The calibration system of the Bdot is shown in Fig.6.8. The procedure is the same as the Ddot calibration except the Bdot readout was recorded instead of the Ddot readout. During the calibration process, the BCS and Bdot were used at the same time at 40 kV applied voltage. The current at the Bdot position can be reconstructed from the BCS readout. As the shunt readout is the current, based on the transmission line theory and assuming the spherical plasma at the anode is equivalent to the open load, the amplitude of the current at the Bdot position is the difference between the forward and reflected current waveform amplitude and the polarity of the current at the Bdot position is the same as the forward current waveform.

Figure 6.10 shows the comparison of the Bdot signal with the BCS signal. All

the waveforms in Figure 6.10 were normalized. According to Figure 6.10, B_{Bdot} is one and C_{Bdot} is zero. The integration of Bdot signal corresponds in good approximation to the shape of the current waveform. The coefficient A_{Bdot} of the Bdot is $(2.85 \pm 0.29) \times 10^9$ A/V which was obtained by dividing the amplitude difference in the forward and reflected current waveform recorded by the BCS by the amplitude of the integrated Bdot signal integral.

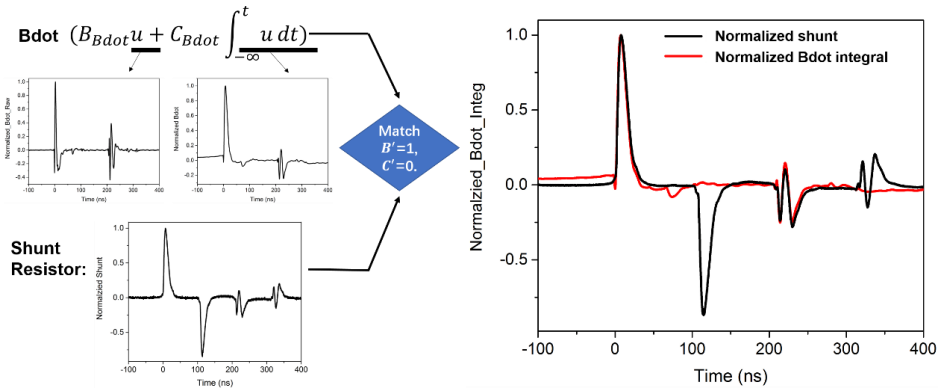

Figure 6.10 Schematic of the Bdot calibration procedure

The summary of all the sensors equations and the coefficients are listed in Table 6.1 below.

Table 6.1 Summary of the calibration result

Sensor Type	Equation	Coefficients
BCS	$I_{HV} = \frac{U_{readout}}{R_{BCS}}$, $V_{HV} = I_{HV}Z_{cable}$	$R_{BCS} = 0.40 \pm 0.04\ \Omega$
Ddot	$V_{HV} = A_{Ddot}\left(B_{Ddot}u + C_{Ddot}\int_{-\infty}^{t} u\,dt\right)$	$A_{Ddot} = (1.30 \pm 0.13) \times 10^{12}$ V/V $B_{Ddot} = 0$, $C_{Ddot} = 1$
Bdot	$I_{HV} = A_{Bdot}\left(B_{Bdot}V_{Bdot} + C_{Bdot}\int_{-\infty}^{t} V_{Bdot}\,dt\right)$	$A_{Bdot} = (2.85 \pm 0.29) \times 10^9$ A/V $B_{Bdot} = 0$, $C_{Bdot} = 1$

6.3.5 Power measurement procedure for discharge in liquid

The principles and theories of the two power measurement methods were introduced in previous sections. In this section, we first present the power measurement by a BCS and the details of separating of the forward and reflected current wave by using a Ddot. Next, the method of employing the Ddot and Bdot is shown to measure the plasma power.

6.3.5.1 BCS Method

A transmission line mounted with BCS is used to deliver power from the FID pulser to a single tungsten pin submerged in a NaCl solution. Since the forward and the reflected waveforms are all present in the BCS measured signal but overlap with each other, the main task of the power measurement is to separate the forward and reflected peaks present in the waveform as shown in Figure 6.11. From transmission line theory, we know that due to reflection, the reflected current has an opposite polarity if the transmission line has an open end, which is applicable for the scenario of the corona discharge in water.

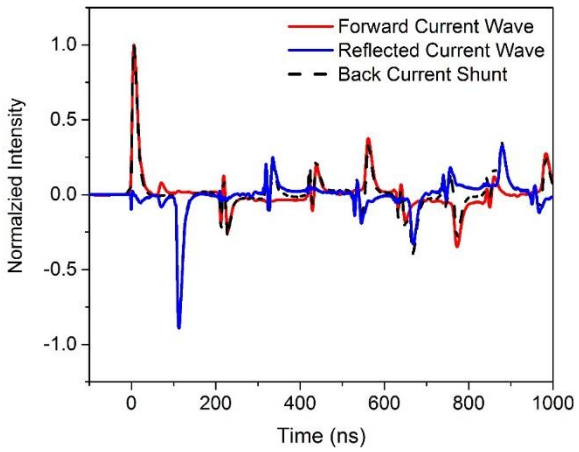

Figure 6.11. The BCS waveform is a superposition of forward and reflected current peak

The time difference between the first peak of the forward waveform and the first peak of the reflected waveform are caused by a different distance that the wave travelled in the transmission line. After passing the BCS position, the forward current wave keeps travelling in the transmission line until it hits the tungsten needle acting as an open end. The reflected current wave with opposite polarity continues to travel in the transmission line but in an opposite direction, passing the BCS. The corresponding signal is captured as the reflected current wave with a time delay. The reflected wave travels an extra distance, which equals to twice the length between the shunt and the tungsten needle. The longer the distance between the BCS and the anode (in this experiment the needle), the clearer separation between the forward and reflected wave is. The situation at the Ddot position is different. Although there is still a difference in time for forward and reflected wave pass the Ddot and trigger signal, the distance from the Ddot to the needle tip is ~10 cm, the time difference between the forward and reflected wave is less than 1 ns. As a result, the forward and reflected voltage wave are in good approximation time-aligned waves at the Ddot position. Assuming the forward and the reflected voltage/current waveform have the same shape, the waveform shape can be retrieved by integrating the signal measured at the Ddot position. By scaling up such waveform shape using the first peak of the forward signal wave captured in the BCS, a time resolved forward signal waveform is retrieved. The reflected waveform is obtained by subtracting the BCS signal waveform from the reconstructed forward waveform. The forward and reflected current waveform are shown in Figure 6.11. Once the forward and reflected current waveforms are obtained from the BCS signal, the power deposition to the plasma can be calculated.

6.3.5.2 Ddot and Bdot Combined Method

As discussed above, the Ddot measures the voltage applied to the discharge and the Bdot measures the current in the transmission line near the electrode. The reconstructed Ddot and Bdot signal represent the overall effect of the time overlapped forward and reflected waveform. After multiplying the measured voltage and current signal after time delay correction, a power waveform is obtained. The power of the pure water discharge is measured using these two methods as a case study reported in the next section. The difference between these two methods is also discussed.

6.4 Case Study

The challenges of studying discharges in liquid are the instabilities of the discharge in time and space. By using the designed discharge in water system together with nanosecond discharge and single pin geometry, the discharge in water has a spherical geometry and is generated at a fixed position near the tip of the tungsten needle as shown in Figure 6.12. It provides convenient features for the optical diagnostics.

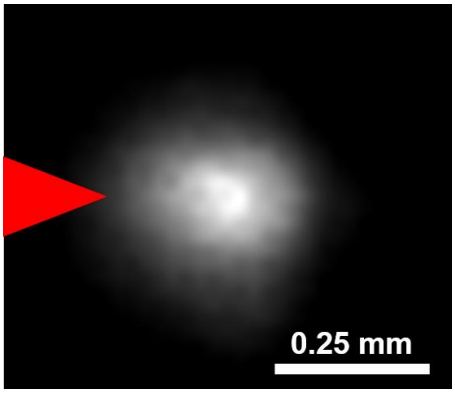

Figure 6.12 The corona discharge in the liquid recorded with an ICCD with an exposure time of 10 ns. Visible emission radius ≈ 150 μm

A 40-kV voltage was applied to the anode and the BCS, Ddot and Bdot signals were recorded at the same time. The power measured by the BCS is shown in Figure 6.13.

We can see that the peak plasma power measured by the BCS is approximately 4 MW, and the energy deposition per pulse is 85 mJ. The energy deposition during the primary power peak (< 20 ns) is approximately half of the energy deposition, the other half of the energy deposition due to the reflections.

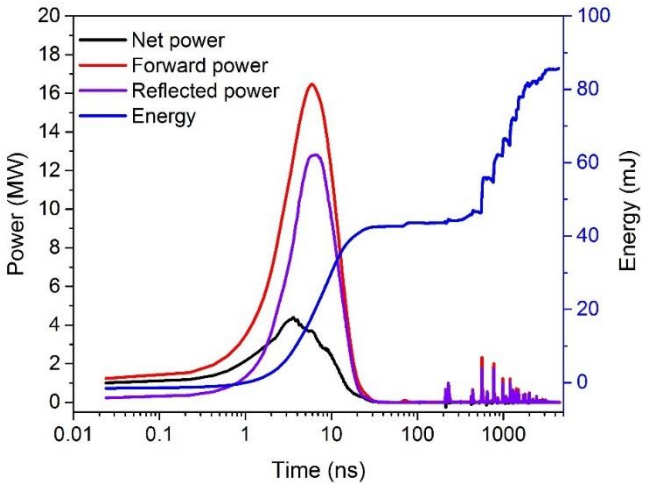

Figure 6.13. The power and energy deposition measured by BCS

The voltage and current measured by the Ddot and Bdot respectively are shown in Figure 6.14. The peak voltage is 55 kV and the corresponding current is 65 A. Multiplying the voltage and current waveform after time delay correction, the power can be obtained, and the energy is the integration of power in the time domain. The power and energy waveforms are shown in Figure 6.15. The peak power is 3.5 MW and the energy obtained is 76 mJ. These values are within 15% of the values obtained by the BCS approach. It is consistent with the 10% uncertainty on the calibrated coefficients.

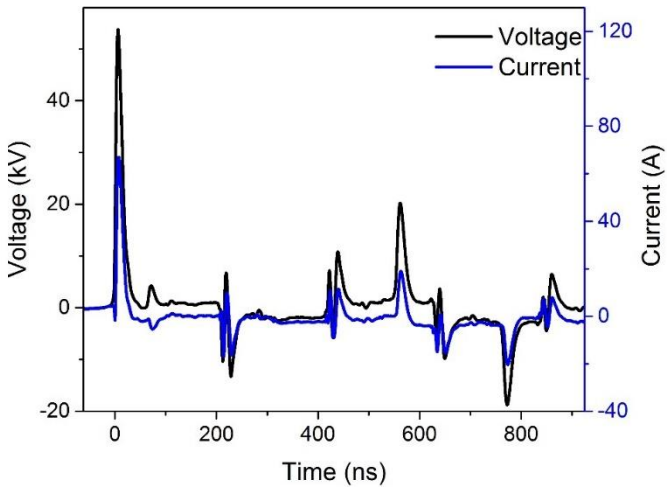

Figure 6.14 Voltage and current measured by Ddot and Bdot respectively

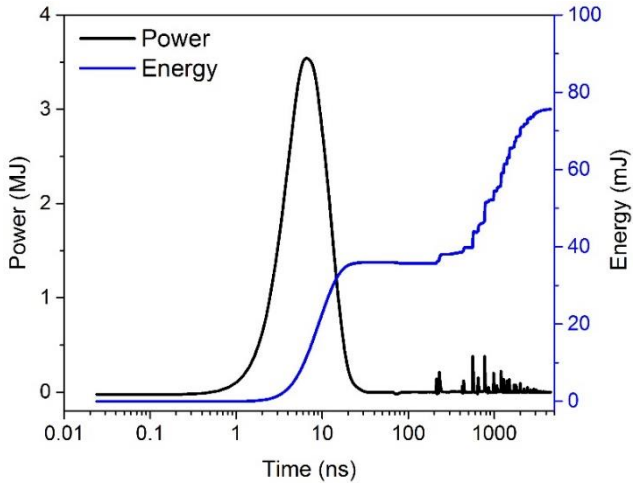

Figure 6.15 Power and energy deposition to discharge in water measured by Ddot and Bdot.

6.5 Conclusion

In this chapter, a time and spatially reproducible discharge was generated in NaCl solution with a conductivity of 200 μS/cm. The discharge was spherical and stayed at the tip of the tungsten needle powered by a nanosecond voltage pulse. The voltage and current of the discharge have been measured by calibrated Back Current Shunt (BCS), Ddot and Bdot.

The BCS was calibrated using a DC voltage supplied with a known resistor in series that allowed to obtain the current. The calibration of the Ddot and Bdot were both performed using calibrated BCS assuming the corona-like plasma generated at the anode is equivalent to open load. The calibration of the sensors yielded uncertainties of 10%.

The power measured by the proposed two different method: BCS and Ddot/Bdot, are within 15% which is similar to the uncertainty in the calibration of the coefficients. This shows the validity of both approaches and the assumptions made to perform the calibration.

7 Conclusion

The aim of this work has been to understand the chemical kinetics of high electron density atmospheric pressure water-containing plasmas. The focus was on Ar-H_2O with water concentration levels from 0.1 to 100%. The water vapor kinetics for these conditions were studied experimentally and by numerical simulations. High electron density atmospheric pressure discharges are usually transient and filamentary. We adapted a pin-to-plate geometry with 9 mm gap and a single pin geometry with grounded outer metal reactor to generate stable discharges in the gas phase and liquid phase respectively. A nanosecond pulse generator producing voltage pulses with rise time of 18 ns and repetition rate of 5 kHz was used to power the gas phase discharge and a nanosecond pulse generator with a faster rise time of 3~5 ns and a lower repetition rate of 1 Hz was used to power the liquid phase discharge. This approach enabled us to achieve reproducible discharges with spatial and temporal control. The stabilization of the plasma filament in the gas phase enabled us to study the time and spatially resolved plasma kinetics on nanosecond time scale.

Laser induced fluorescence (LIF) was used to measure the absolute OH density in the plasma discharge and in addition previously reported two photon absorption laser induced fluorescence (TaLIF) was used to measure the absolute H density. The calibration to obtain absolute densities was Rayleigh scattering and using Kr TaLIF respectively. A global model *Globalkin* was used as a plasma kinetics solver and a previously reported chemical reaction set for argon water air mixture was used with some modification and additions required for the new plasma conditions. The input parameters such as power, discharge volume and gas composition were measured by electrical

measurements, imaging and OH fluorescence decay time measurements respectively. The plasma kinetics model was validated by the measured time-resolved H and OH densities. The dominant reaction kinetics has been studied for the main radical species such as H, OH and O during the discharge and in the afterglow. This was complemented with the formation of long-lived species (H_2, H_2O_2). The kinetics study has been mainly focused on the core of the discharge (0-D kinetics). To assess radial transport in plasma filaments, additional measurements of temporal and spatially resolved species densities were performed. The validated argon water reaction set for high electron density low water concentration discharges was extended to the pure water vapor environment. A modification of the chemical reaction rates to accommodate the higher gas temperature (in excess of 1000 K) was implemented. While the fast and intensive gas heating and pressure changes have not been implemented in detail in the model, we used a two-stage simulation approach to consider the shock wave effect assuming fast pressure relaxation. The modified argon water kinetics proved suitable for predicting reported experimentally measured long-lived species production in pure water vapor discharges and accurately captured the reported plasma properties including the electron density and gas temperature.

Two systems were developed to generate spatially and temporally reproducible discharges in a bubble and directly in liquid. Experimental studies were conducted in a synchronized pulsed bubble discharge system and a corona liquid discharge system to provide more insight about the high electron density water-containing plasma behavior at high water concentrations (> 1%). The morphology and memory effect were studied in the bubble system by electrical measurements and fast imaging. In the corona liquid discharge system, a set of homemade sensors, including voltage and current sensors,

were developed and integrated into the plasma reactor to achieve fast response time, good electromagnetic shielding and accurate power measurements. A procedure of the power measurement was developed for liquid corona discharge.

The key conclusions of this thesis are:

1. In the high specific energy discharges, the H and O are two main radicals in the discharge and afterglow. In this scenario, the production of H_2, O_2 and H_2O are favored rather than H_2O_2 due to the fast recombination reaction rates in the reactions producing them. To increase the density and selectivity of H_2O_2 and OH, the specific energy should be small. Traditionally, OH is considered to be a dominant radical, however for higher specific energies, present in many plasmas at atmospheric pressure, O and H radical seem to be dominant.

2. In nanosecond pulsed high election density water-containing atmospheric pressure plasmas, the dominant production reactions of H and OH are charge exchange and electron-ion recombination reactions. The three-body recombination with H and O are the main source of consumption for H. The consumption mechanism for OH is different during the discharge and in the afterglow. During the discharge, OH is mainly consumed by electron-induced dissociation; while in the afterglow, OH reacting with H and O are more dominant.

3. A local minimum in the OH fluorescence radial distribution has been observed in both the dry and humid shielding case of the argon water plasma jet at the time scale of 5 μs which is much longer than the reported similar phenomenon during the ionizing phase of the nanosecond pulsed

plasma attributed to ionic induced reactions at sub microsecond timescales. Results indicate that diffusion of H and O from the core to the surrounding in the afterglow can enhance this pattern by producing OH in the surrounding of the discharge where the radical density is lower and the OH lifetime is also longer than in the core.

4. Discharges in bubbles have many similarities with gas phase dielectric barrier discharges. The surface charge accumulated on the surface of a gas supplying quartz tube is shown to be responsible for the reducing ignition power observed in the memory effect of pulsed bubble system. The transition from a diffuse to a filamentary discharge in the bubble proceeds similarly as glow-to-spark transitions observed in the gas phase discharge.

5. The power deposition in the nanosecond corona discharge in the liquid water is well captured by calibrated home-made voltage (Ddot) and current (Bdot) sensor in nanosecond time resolution. The difference between the power depositions measured by two different approaches is within 15%. This accurate power measurement is invaluable as input of models to gain more insight in plasmas generated directly in the liquid phase.

In conclusion, we have developed and studied a series of different water-containing discharges to increase the current understanding of the plasma kinetics in such discharges. All the discharges in this study are designed to be high electron density and filamentary as the discharges used for environmental remediation in real world applications. Due to the challenges related to conducting experimental measurements of bubble and liquid water discharge caused by fraction and phase change, time-resolved laser diagnostics were applied to the gas phase discharge with similar plasma properties as

discharges in bubbles and directly in liquid water. The developed bubble and direct liquid water discharge reactor with preliminary characterization will allow for the development of more accurate and detailed measurements in the future which will without doubt increase further our understanding of these discharges.

Bibliography

[1] Bruggeman P. J. Iza F. and Brandenburg R. (2017) Foundations of atmospheric pressure non-equilibrium plasmas Plasma Sources Sci. Technol. **26** 123002

[2] Dorai R. and Kushner M. J. (2003) A model for plasma modification of polypropylene using atmospheric pressure discharges *J. Phys. D: Appl. Phys.* **36** 666

[3] Van Veldhuizen E. M. (20000 *Electrical Discharges for Environmental Purposes: Fundamentals and Applications* (Huntington, NY: Nova Science)

[4] Chang J. S. (2001) Recent development of plasma pollution control technology: a critical review *Sci. Technol. Adv. Mater.* **2** 571–6

[5] Malik M. A. (2010) Water purification by plasmas: which reactors are most energy efficient? *Plasma Chem. Plasma Process* **30** 21–31

[6] Locke B. R., Sato M., Sunka P., Hoffmann M. R. and Chang J. S. (2006) Electrohydraulic discharge and nonthermal plasma for water treatment. Industrial & Engineering Chemistry Research **45** 882-905

[7] Kolb J. F., Joshi R. P., Xiao S. and Schoenbach K. H. (2008) Streamers in water and other dielectric liquids *J. Phys. D: Appl. Phys.*, **41**, 234007

[8] An W., Baumung K. and Bluhm H. (2007) Underwater streamer propagation analyzed from detailed measurements of pressure release *J. Appl. Phys.,* **101**, 053302

[9] Bruggeman J. P. and Locke R. B. (2013) Assessment of potential applications of plasma with liquid water, chapter in *Low Temperature Plasma Technology: Methods and Applications*, eds. Chu P and Lu X P, CRC Press, New York.

[10] Bruggeman P. J. *et al* (2016) Plasma–liquid interactions: a review and roadmap *Plasma Sources Sci. Technol.* **25** 053002

[11] Bruggeman P. J. and Leys C. (2009) Non-thermal plasmas in and in contact with liquids *J. Phys. D: Appl. Phys.* **42** 053001

[12] Dobrynin D., Seepersad Y., Pekker M., Shneider M., Friedman G. and Fridman A. (2013) Non-equilibrium nanosecond-pulsed plasma generation in the liquid phase (water, PDMS) without bubbles: fast imaging, spectroscopy and leader-type model. *J. Phys. D: Appl. Phys.* **46**, 105201

[13] Sainct F. P., Lacoste D. A., Kirkpatrick M. J., Odic E. and Laux C. O. (2014) Temporal evolution of temperature and OH density produced by nanosecond repetitively pulsed discharges in water vapour at atmospheric pressure *J. Phys. D: Appl. Phys.* **47** 075204

[14] Luo Y., Lietz A. M., Yatom S., Kushner M. J. and Bruggeman P. J. (2019) Plasma kinetics in a nanosecond pulsed filamentary discharge sustained in Ar-H_2O and H_2O *J. Phys. D: Appl. Phys.* **52** 044003

[15] Van Gaens W. and Bogaerts A. (2013) Kinetic modelling for an atmospheric pressure argon plasma jet in humid air *J. Phys. D: Appl. Phys.* **46** 275201

[16] Yatom S., Luo Y., Xiong Q. and Bruggeman P. J. (2017) Nanosecond pulsed humid Ar plasma jet in air: shielding, discharge characteristics and atomic hydrogen production *J. Phys. D: Appl. Phys.* **50** 415204

[17] Wende K., Williams P., Dalluge J. et al (2015) Identification of the biological active liquid chemistry induced by a nonthermal atmospheric pressure plasma jet, *Biointerphases* **10,** 029518

[18] Magureanu M., Piroi D., Mandache N.B., David V., Medvedovici A. and Parvulescu V.I. (2010) Degradation of pharmaceutical compound pentoxifylline in water by non-thermal plasma treatment, *Water Research* **44**, 3445–3453

[19] Chu P. K., Chen J. Y., Wang L. P. and Huang N. (2002) Plasma-surface modification of biomaterials *Mater. Sci. Eng. R Rep.* **36** 143-206

[20] Ju Y. and Sun W. (2015) Plasma assisted combustion: Dynamics and

chemistry *Prog. Energy Combust. Sci.* **48** 21-83

[21] Liu D.X., Bruggeman P.J., Iza F., Rong M.Z. and Kong M.G. (2010) Global model of low-temperature atmospheric-pressure He + H_2O plasmas, *Plasma Sources Sci. Technol.* **19,** 025018

[22] Stalder K.R., Vidmar R.J., Nersisyan G. and Graham W.G. (2006) Modeling the chemical kinetics of high-pressure glow discharges in mixtures of helium with real air, *J. Appl. Phys.* **99,** 09330

[23] Vasko C.A., Liu D.X., van Veldhuizen E.M., Iza F. and Bruggeman P.J. (2014) Hydrogen Peroxide Production in an Atmospheric Pressure RF Glow Discharge: Comparison of Models and Experiments, *Plasma Chem and plasma Process* **34,**1081-1099

[24] Verreycken T., Sadeghi N. and Bruggeman P.J. (2014) Time-resolved absolute OH density of a nanosecond pulsed discharge in atmospheric pressure He–H_2O: absolute calibration, collisional quenching and the importance of charged species in OH production, *Plasma Sources Sci. Technol.* **23,** 045005

[25] Verreycken T., Mensink R., van der Horst R., Sadeghi N. and Bruggeman P.J. (2013) Absolute OH density measurements in the effluent of a cold atmospheric-pressure Ar–H_2O RF plasma jet in air, *Plasma Sources Sci. Technol.* **22,** 055014

[26] Lietz A.M. and Kushner M.J. (2016) Air plasma treatment of liquid covered tissue: long timescale chemistry, *J. Phys. D: Appl. Phys.* **49,** 425204

[27] Nikiforov A. Yu, Sarani A. and Leys C. (2011) The influence of water vapor content on electrical and spectral properties of an atmospheric pressure plasma jet *Plasma Sources Sci. Technol.* **20** 015014

[28] Chang J., Urashima K. and Uchida Y. (2002) Characteristics of pulsed arc electrohydraulic discharges and their application to water treatment *Res. Rep. Tokyo Denki Univ.* **50** 1–12

[29] Korobeinikov S., Melekhov A. and Besov A. (2002) Breakdown initiation in water with the aid of bubbles *High Temp.* **40** 652–9

[30] Starikovskiy A., Yang Y., Cho Y. and Fridman A. (2011) Non-equilibrium plasma in liquid water: dynamics of generation and quenching *Plasma Source Sci. Technol.* **20** 024003

[31] Mededovic S. and Locke B.R. (2007) Primary chemical reactions in pulsed electrical discharge channels in water, *J. Phys. D: Appl. Phys.* **40,** 7734

[32] Sainct F. Thesis

[33] Sainct F., Lacoste D., Kirkpatrick M., Odic E. and Laux C. O. (2012) Experimental study of nanosecond repetitively pulsed discharges in water vapor *Int. J. Plasma Environ. Sci. Technol.* **6** 125–9

[34] https://kinetics.nist.gov/kinetics/index.jsp

[35] http://combustion.berkeley.edu/gri-mech/version30/text30.html

[36] Malik M. A., Ghaffar A. and Malik S. A. (2001) Water purification by electrical discharge, *Plasma Sources Sci. Technol.* **10** 82

[37] Anpilov A. M., Barkhudarov E. M., Bark Yu B., Zadiraka Yu V., Christofi M., Kozlov Yu N., Kossyi I A., Kop'ev V A., Silakov V. P., Takatakishvili M. I. and Temchin S. M. (2001) Electric discharge in water as a source of UV radiation, ozone and hydrogen peroxide, *J. Phys. D: Appl. Phys.* **34** 993-999

[38] Magureanu M., Mandache N. B., Bradu C. and Parvulescu V. I. (2018) High efficiency plasma treatment of water contaminated with organic compounds. Study of the degradation of ibuprofen, *Plasma Process. Polym.* **15** 1700201

[39] Shih K. and Locke B. R. (2010) Chemical and physical characteristics of pulsed electrical discharge within gas bubbles in aqueous solutions, *Plasma Chem. Plasma Process.* **30** 1-20

[40] Miichi T., Ihara S., Satoh S. and Yamabe C. (2000) Spectroscopic measurements of discharges inside bubbles in water, *Vacuum* **59** 236-243

[41] Smirnov B. M., Babaeva N. Y., Naidis G. V., Panov V. A., Saveliev A. S., Son E. E. and Tereshonok D. V. (2018) The bubble method of water purification, *Europhys. Lett.* **121** 48007

[42] Sommers B. S. and Forster J. E. (2014) Plasma formation in underwater gas bubbles, *Plasma Sources Sci. Technol.* **23** 015020

[43] Hamdan A. and Cha M. S. (2015) Ignition modes of nanosecond discharge with bubbles in distilled water, *J. Phys. D: Appl. Phys.* **48** 405206

[44] Tachibana K., Takekata Y., Mizumoto Y., Motomura H. and Jinno M. (2011) Analysis of a pulsed discharge within single bubbles in water under synchronized conditions, *Plasma Sources Sci. Technol.* **20** 034005

[45] Vanraes P., Nikiforov A. and Leys C. (2012) Electrical and spectroscopic characterization of underwater plasma discharge inside rising gas bubble, *J. Phys. D: Appl. Phys*. **45** 245206

[46] Tian W., Tachibana K. and Kushner M.J. (2014) Plasmas sustained in bubbles in water: optical emission and excitation mechanisms, *J. Phys. D: Appl. Phys.* **47,** 055202

[47] Bruggeman P., Leys C. and Vierendeels J. (2007) Experimental investigation of dc electrical breakdown of long vapour bubbles in capillaries, *J. Phys. D: Appl. Phys.* **40** 1937-1943

[48] Bruggeman P., Verreycken T., Gonzalez M. A., Walsh J. L., Kong M. G., Leys C. and Schram D. C. (2010) Optical emission spectroscopy as a diagnostic for plasmas in liquids: Opportunities and pitfalls, *J. Phys. D: Appl. Phys.* **43** 124005

[49] Takeuchi N., Ishii Y. and Yasuoka K. (2012) Modeling chemical reactions in dc plasma inside oxygen bubbles in water, *Plasma Sources Sci. Technol.* **21** 015006

[50] Iza F., Walsh J. and Kong M. (2009) From Submicrosecond-to Nanosecond-Pulsed Atmospheric-Pressure Plasmas, *IEEE Trans. Plasma Sci.*

37 1289-1296

[51] Nijdam S., Takahashi E., Markosyan A. H. and Ebert U. (2014) Investigation of positive streamers by double-pulse experiments, effects of repetition rate and gas mixture, *Plasma Sources Sci. Technol.* **23** 025008

[52] Huang B., Carbone E., Takashima K., Zhu X., Czarnetzki U. and Pu Y. (2018) The effect of the pulse repetition rate on the fast ionization wave discharge, *J. Phys. D: Appl. Phys.* **51** 225202

[53] Babaeva N. Y. and Kushner M. J. (2009) Structure of positive streamers inside gaseous bubbles immersed in liquid, *J. Phys. D: Appl. Phys.* **42** 32003

[54] Vanraes P., Nikiforov A., Lessiak M. and Leys C. (2012) Time-resolved characterization of a pulsed discharge in a stationary bubble, *J. Phys.: Conf. Ser.* **406** 012013

[55] Bayle P., Bayle M. and Forn G. (1985) Neutral heating in glow to spark transition in air and nitrogen, *J. Phys. D: Appl. Phys.* **18** 2395–415

[56] Rep'ev A. G., Repin P. B. and Danchenko N. G. (2007) Transition of an atmospheric-pressure glow discharge from the diffuse to spark phase, *Tech. Phys. Lett.* **33** 1011–14

[57] Akishev Yu, Grushin M., Kochetov I., Karal'nik V., Napartovich A. and Trushkin N. (2005) Negative corona, glow and spark discharges in ambient air and transitions between them, *Plasma Sources Sci. Technol.* **14** S18–25

[58] Korolev Yu D., Frants O. B., Landl N. V., Geyman V. G. and Matveev I. B. (2007) Glow-to-spark transitions in a plasma system for ignition and combustion control, *IEEE Trans. Plasma Sci.* **35** 1651–7

[59] Chalmers I. D. and Duffy H. (1971) Observations of the arc-forming stages of spark breakdown using an image intensifier and converter, *J. Phys. D: Appl. Phys.* **4** 1302–5

[60] Suleebka P., Barrault M. R. and Craggs J. D. (1975) Constriction of a high pressure glow discharge in hydrogen, *J. Phys. D: Appl. Phys.* **8** 2190–7

[61] Bruggeman P., Guns P., Degroote J., Vierendeels J. and Leys C. (2008) Influence of the water surface on the glow-to-spark transition in a metal-pin-to-water electrode system, *Plasma Sources Sci. Technol.* **17** 045014

[62] Walsh J. and Bruggeman P. (2011) Filamentation of diffuse He-H_2O atmospheric pressure glow discharges in a metal pin-water electrode geometry, *IEEE Trans. Plasma Science* **39** 11

[63] Babaeva N. Y., Naidis G. V. and Kushner M. J. (2018) Interaction of positive streamers in air with bubbles floating on liquid surfaces: conductive and dielectric bubbles, *Plasma Sources Sci. Technol.* **27** 015016

[64] Sharma A., Levko D., Raja L. and Cha M. S. (2016) Kinetics and dynamics of nanosecond streamer discharge in atmospheric-pressure gas bubble suspended in distilled water under saturated vapor pressure conditions, *J.Phys.D: Appl. Phys.* **49** 395205

[65] Saville D. A. (1997) Electrodynamics, The Tayler-Melcher Leaky Dielectric Model, *Ann. Rev. Fluid. Mech.* **24** 27-64

[66] Crank J. (1980) The Mathematics of Diffusion 2nd edition, *Oxford University Press*

[67] Schwertz F. A. and Brow J. E. (1951) Diffusivity of Water Vapor in Some Common Gases, *J. Chem. Phys.* **19** 640

[68] Celestin S., Canes-Boussard G., Guaitella O., Bourdon A. and Rousseau A. (2008) Influence of the charges deposition on the spatio-temporal self-organization of streamers in a DBD, *J. Phys. D: Appl. Phys.* **41** 205214

[69] Akishev Y., Aponin G., Balakirev A., Grushin M., Karalnik V., Petryakov A. and Trushkin N. (2011) 'Memory' and sustention of microdischarges in a steady-state DBD: volume plasma or surface charge? *Plasma Sources Sci. Technol.* **20** 024005

[70] Zhang P. and Kortshagen U. (2006) Two-dimensional numerical study of atmospheric pressure glows in helium with impurities, *J. Phys. D: Appl. Phys.*

39 153–163

[71] Jánský J., Le Delliou P., Tholin F., Tardiveau P., Bourdon A. and Pasquiers S. (2011) Experimental and numerical study of the propagation of a discharge in a capillary tube in air at atmospheric pressure, *J. Phys. D: Appl. Phys.* **44** 335201

[72] Ellis H. W., McDanniel E. W., Albritton D. L., Viehland L. A., Lin S. L. and Mason E. A. (1978) Transport properties of gaseous ions over a wide energy range. Part II, *Atomic Data and Nuclear Data Tables* **22** 179-217

[73] Sakiyama Y., Graves D.B., Chang H.W., Shimizu T. and Morfill G.E. (2012) Plasma chemistry model of surface microdischarge in humid air and dynamics of reactive neutral species, *J. Phys. D: Appl.Phys.* **45,** 425201

[74] Celestin S., Allegraud K., Canes-Boussard G., Leick N., Guaitella O. and Rousseau A. (2008) Pattern of Plasma Filaments Propagating on a Dielectric Surface, *IEEE Trans. Plasma Sci.* **36**, 1326–1327

[75] Emelyanov O. A. and Shemet M. V. (2014) Single dielectric barrier discharge characteristics in needle-to-plane configuration, *J. Phys. D: Appl. Phys.* **47** 315201

[76] Seepersad Y., Fridman A. and Dobrynin D. (2015) Anode initiated impulse breakdown in water: the dependence on pulse rise time for nanosecond and sub-nanosecond pulses and initiation mechanism based on electrostriction *J. Phys. D: Appl. Phys.* **48** 424012

[77] Vasilyak L. M. and Krasnochub A. V. (2013) Method for Measuring the Absorbed Energy in nanosecond Electric Discharges *Surf. Eng. Appl. Electrochem,* **49**, No.5, 427-432.

[78] Klochko A. V., Starikovskaia S. M., Xiong Z. and Kushner M. J. (2014) Investigation of capillary nanosecond discharges in air at moderate pressure: comparison of experiments and 2D numerical modelling *J. Phys.D: Appl. Phys* **47**, 365202.

[79] Huiskamp T., Beckers F. J. C. M., van Heesch E. J. M. and Pemen A. J. M. (2016) B-Dot and D-Dot Sensors for (Sub)Nanosecond High-Voltage and High-Current Pulse Measurements *IEEE Sens. J.* **16**, 10.

Appendix 1

After pressure relaxation, we assume the pressure goes back to 1 atm. The process of the plasma channel expansion is assumed to be equivalent to the movement of a piston-cylinder system.

$$U_0 = U_1 + P_{atm}(V_1 - V_0) + \frac{mc^2}{2} \quad (1)$$

U_0 and U_1 are the internal energy of the plasma channel before and after the shock wave relaxation, V_0 and V_1 are the volume of the plasma channel before and after the shock wave relaxation, P_{atm} is the atmospheric pressure, m is the mass of the mixture in the plasma channel, c is the speed of sound at the plasma channel temperature before the shock wave relaxation. Combining the flow work ($P_{atm}V_0$ and $P_{atm}V_1$) with the internal energy, we obtain the enthalpy energy from equation (2). H_0 and H_1 are the enthalpy of the gas mixture in the plasma volume before and after the shock wave pressure relaxation. m, γ_{mix} and R_{mix} are the mass, specific heat ratio and gas constant of the gas mixture in the plasma volume.

$$H_0 = H_1 + \frac{m\gamma R_{mix} T_0}{2} \quad (2)$$

$$H_0 = \left(\sum_i c_{p_{i0}} N_i\right) T_0$$

$$H_1 = \left(\sum_i c_{p_{i0}} N_i\right) T_1$$

$$m = \sum_i M_i N_i$$

$$\gamma_{mix} = \frac{\sum_i c_{p_{i0}} N_i}{\sum_i c_{v_{i0}} N_i}$$

$$R_{mix} = \frac{\sum_i R_i N_i}{\sum_i N_i}$$

N_i is the number of particles in species i. The number of particles for different species (N_i) are taken from the global model simulation result. T_0 is the gas temperature before the shock wave relaxation, and T_1 is the gas temperature after the shock wave relaxation. $c_{p_{i0}}$ is the constant pressure heat capacity for species i before the shock wave relaxation and $c_{p_{i1}}$ is the constant pressure heat capacity for species i after the shock wave relaxation. The values of the specific heat of species after the shock wave relaxation are assumed to be the same as the ones before the shock wave relaxation since the variation of the specific heat due to gas temperature between 2000 and 3000 K is small. The properties of different species are taken from the Engineering toolbox*. M_i is the mass of a particle for species i.

The constant volume calculation yields T_g = 2167 K at 94.6 ns and equation (2) yields T_1 = 1607 K.

* www.engineeringtoolbox.com

Appendix 2

According to the constant volume calculation, the gas composition in the plasma channel mainly consists of 41.3% H, 24% O, 16 % H_2, 5.2% O_2, 4.2 % OH and 2.5% H_2O at gas temperature of 2083 K when t = 40.6 ns. And the gas composition mainly consists of 37% H, 28% O, 25% H_2, 5.7% O_2, 2.4% OH and 0.78% H_2O at gas temperature of 2167 K when t = 94.6. The relaxation time is calculated by dividing the plasma radius (R_{plasma}) by the speed of sound as in Equation 3, where γ_{mix} and R_{mix} are the specific heat ratio and gas constant of the gas mixture. And plasma channel has a radius of 100 μm.

$$\tau = \frac{R_{plasma}}{\sqrt{\gamma_{mix} R_{mix} T}} \quad (3)$$

$$\gamma_{mix} = \frac{\sum_i c_{p_{i0}} N_i}{\sum_i c_{v_{i0}} N_i}$$

$$R_{mix} = \frac{\sum_i R_i N_i}{\sum_i N_i}$$

$c_{p_{i0}}$ is the constant pressure heat capacity for species i before the shock wave relaxation and $c_{v_{i0}}$ is the constant volume heat capacity for species i before the shock wave relaxation. N_i is the number of particles in species I. R_i is the gas constant for species i. By using these values, equation 3 yields shock wave relaxation time of 54 ns and 52 ns at at t = 40.6 ns and 94.6 ns respectively.